UNIVERSIDAD DE CHILE
FACULTAD DE CIENCIAS FÍSICAS Y MATEMÁTICAS
DEPARTAMENTO DE FÍSICA

EXPERIMENTAL STUDY ON DYNAMIC HYPERUNIFORM STATES

TESIS PARA OPTAR AL GRADO DE
MAGÍSTER EN CIENCIAS, MENCIÓN FÍSICA

JUAN CARLOS ANTONIO SOBARZO PONCE

PROFESOR GUÍA:
NICOLÁS MUJICA FERNÁNDEZ
PROFESOR CO-GUÍA:
GUSTAVO EMILIO CASTILLO BAUTISTA

MIEMBROS DE LA COMISIÓN:
DENISSE ELIZABETH DEL CARMEN PASTÉN GUZMÁN
RODRIGO ANTONIO SOTO BERTRÁN
SCOTT RUSSELL WAITUKAITIS

SANTIAGO DE CHILE
2019

RESUMEN DE LA TESIS PARA OPTAR AL GRADO
DE MAGÍSTER EN CIENCIAS, MENCIÓN FÍSICA
POR: Juan Carlos Antonio Sobarzo Ponce
FECHA: 02/07/19
PROF. GUÍA: Nicolás Mujica Fernández
PROF. CO-GUÍA: Gustavo Emilio Castillo Bautista

ESTUDIO EXPERIMENTAL DE ESTADOS DINÁMICAMENTE HIPERUNIFORMES

Esta tesis consiste en un estudio experimental de estados dinámicamente hiperuniformes, llevado a cabo mediante la caracterización de las fluctuaciones de densidad en un sistema granular vibrado de geometría cuasi-bidimensional. El Capítulo 1 consta de una introducción al concepto de hiperuniformidad, así como una revisión de los trabajos previos en este tema y sus aplicaciones. De manera adicional, se exponen las características fundamentales de los medios granulares y su reciente vinculación con el estudio de sistemas hiperuniformes. En el Capítulo 2 se presenta la descripción de las fluctuaciones de densidad mediante la varianza del número de partículas y el factor de estructura, y posteriormente, la definición formal de hiperuniformidad a través de estas cantidades. En el Capítulo 3, con el propósito de estudiar el transporte de granos en el experimento, introducimos el coeficiente de difusión y su relación con el desplazamiento cuadrático medio, además de incluir una breve discusión sobre el concepto de temperatura granular. Estos dos últimos capítulos representan el fundamento teórico de esta investigación, que nos permite describir el sistema en estudio y analizar los resultados experimentales obtenidos posteriormente. El Capítulo 4 consta de una descripción detallada del montaje experimental y de los métodos experimentales utilizados, específicamente la detección de partículas y el seguimiento de sus trayectorias. Además, en el Capítulo 5 se incluyen resultados de trabajos previos en este mismo montaje que son útiles para el posterior análisis de nuestros resultados, tales como la existencia de una transición de fase de tipo líquido-sólido y los parámetros de orden que permiten describirla. En el Capítulo 6 se exponen los resultados experimentales y su posterior discusión. En específico, se muestra que la varianza del número de partículas no es un parámetro idóneo para caracterizar hiperuniformidad en nuestro montaje, debido a efectos de tamaño finito. Es más, la varianza del número de partículas puede dar indicaciones erróneas de hiperuniformidad en un sistema finito. Sin embargo, el factor de estructura permite observar la supresión de las fluctuaciones de densidad a gran escala que caracteriza a un estado hiperuniforme, y demuestra ser robusto con respecto al tamaño del sistema. De forma adicional, se presenta brevemente el modelo teórico propuesto por nuestros colaboradores, Rodrigo Soto y Néstor Sepúlveda, basado en una hipótesis que otorga una posible explicación al origen de los estados hiperuniformes generados dinámicamente en este sistema. La solución numérica de este modelo reproduce los resultados experimentales, en particular la presencia de hiperuniformidad en el punto crítico. Finalmente, en el Capítulo 7 se presentan las conclusiones más relevantes de esta tesis, además de propuestas para investigaciones futuras que puedan continuar y complementar este trabajo.

Abstract

This thesis consists of an experimental study on dynamic hyperuniformity, carried out through the characterization of density fluctuations in a vibrated granular setup of quasi-bidimensional geometry. In Chapter 1 we introduce the concept of hyperuniformity, and review previous work on this subject and its applications. Additionally, we present the fundamental features of granular media, and their recent relevance in the study of hyperuniform systems. Chapter 2 introduces the description of density fluctuations through the particle number variance and the structure factor, and the formal definition of hyperuniformity through these quantities. In Chapter 3, with the aim of studying transport of the grains in the experiment, we introduce the diffusion coefficient and its relation to the mean square displacement of particles, and make a brief discussion on the concept of granular temperature. These last two chapters represent the theoretical background for this research, which allows us to describe the system under study and analyze subsequently the experimental results obtained. In Chapter 4 we present a detailed description of the experimental setup and the experimental methods used, specifically, particle detection and tracking of their trajectories. Furthermore, in Chapter 5 we include results from previous work on this same setup, such as the existence of a liquid-to-solid-like phase transition and the order parameters that describe it. These previous results are useful for the subsequent analysis of our data. Chapter 6 comprises our experimental results and the ensuing discussion. Specifically, we show that the particle number variance is not a well-suited parameter in order to characterize hyperuniformity in our setup, due to finite size effects. Moreover, the particle number variance can give erroneous indications of hyperuniformity for finite size systems. On the other hand, the structure factor allows us to observe the suppression of density fluctuations at large scales, characteristic of a hyperuniform state, and proves to be robust to the system size. Additionally, we briefly illustrate the theoretical model proposed by our collaborators, Rodrigo Soto and Nestor Sepulveda, based on a hypothesis that provides a possible explanation to the origin of hyperuniform states generated dynamically in this experiment. Numerical solution of this model reproduces the experimental results, particularly the presence of hyperuniformity. Finally, in Chapter 7 we present the most relevant conclusions of this thesis, as well as a perspective on future research that could complement and give continuity to this work.

Agradecimientos

Primero que todo, agradezco a mi familia por todo el amor y apoyo incondicional que siempre me han entregado. Gracias a mi viejo, por darlo todo por mí y por ser un ejemplo de esfuerzo y perseverancia. Sin ti, jamás hubiera llegado hasta aquí. Gracias a mi mamita, por todo lo que me has inculcado, sobretodo por enseñarme el valor de la responsabilidad y la confianza en uno mismo. Gracias a mi hermana, Dangella, mi mejor amiga. Gracias por escucharme, aconsejarme y contenerme en los momentos difíciles. Gracias por todas esas llamadas telefónicas, y por hacerme reír cuando estoy triste.

Gracias a todas mis amigas y amigos. Primero, gracias a Catalina por ser un ejemplo de amistad. Gracias por todo, son muchas cosas que no caben en esta página. Gracias Caro, por todo tu cariño y consejos, gracias por tu amistad y por todos los momentos, alegres y tristes, que hemos compartido. Gracias Mariana, amiga querida, por tu sabiduría y por darme otra perspectiva de la ciencia. Gracias Rocío por tu generosidad, preocupación y cariño. Gracias Javier, que me conoces tanto, por tu apoyo y sinceridad.

Gracias a toda la bonita gente que conocí trabajando en el LMFE. Gracias a Gustavo, por ser mi co-guía en esta tesis. Yo creo que no te das cuenta lo mucho que me has enseñado. Gracias a ti y a Pablo por darme la oportunidad de trabajar y hacer clases con ustedes en Rancagua. Me ayudó a descubrir el gusto por la docencia. Gracias a Antonella, Vicente y Héctor, por compartir su experiencia y conocimientos. Gracias por todos esos almuerzos que compartimos, gracias por su generosidad. Gracias también a Belén, por ser tan preocupada y atenta.

Thanks also to Scott. It has been a pleasure to meet you, and I am looking forward to working together. Thanks for all your support when I was applying to a PhD.

Por último, gracias a Nico, mi profesor guía. Sin tu apoyo no hubiera podido continuar mis estudios. Gracias por todo, gracias enseñarme tanto y en especial por la comprensión y la paciencia. Gracias por darme la oportunidad de trabajar contigo y de dar mis primeros pasos en la física experimental.

Esta tesis fue financiada gracias a los proyectos Fondecyt 1150393 y QUIMAL 160001.

Contents

Chapter 1

Introduction

One of the most remarkable human abilities is pattern recognition: the cognitive process that matches a perceived stimulus with information retrieved from memory. Our brains are constantly identifying order, shapes and structures everywhere we look. This phenomenon is so persistent that it can be misleading, making us see a familiar pattern where there is none. In 1976, Viking 1 spacecraft, part of NASA's Viking program, took images of Mars surface in the region called Cydonia. One of the images taken captured the public eye because it bore a striking resemblance to a human face (see Figure 1.1a). This led many people to believe that the structure was the remnant of an alien civilization. Later on, higher resolution images proved it was just a trick of light and shadows. The Italian painter Giuseppe Arcimboldo (1527-1593) is widely known for producing paintings of simple objects, like fruits, vegetables, flowers or books, but arranged in such a way that gives them the appearance of human heads (see Figure 1.1b). In psychology, the term *pareidolia* is used to describe the phenomenon in which the mind responds to a vague, random stimulus by mistakenly perceiving a familiar pattern.

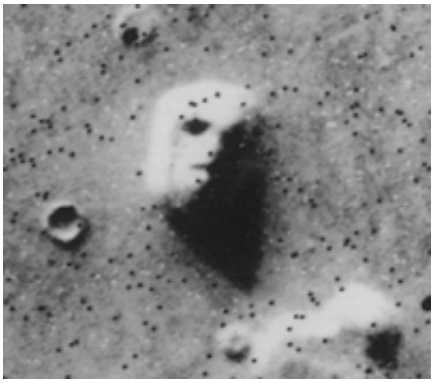

(a)

(b)

Figure 1.1: Pareidolia. (a) Viking 1 processed image of the "Face on Mars", a hill in the region of Cydonia in Mars, with the appearance of a humanoid face. Cropped image from NASA, public domain. (b) The fruit basket, by Giuseppe Arcimboldo (*c.* 1590), public domain. Inverting the painting it displays a fruit basket, but the orientation intentionally given by the artist shows the resemblance of an anthropomorphic face.

But what happens when there is actually a pattern, a hidden order that we are just not able to identify? Particularly in physics, we have been studying how matter is structured for centuries. We have categorized it, among other criteria, according to the degree of order of its components. We know atoms in a crystalline solid are ordered in a periodic lattice, while in an amorphous solid, they have no long-range order. In the early 2000s, professor Salvatore Torquato from Princeton University started studying point configurations and density fluctuations of *hyperuniform states*: systems that, regardless of their degree of local order, look extremely uniform at large scales [1]. Regular lattices naturally fall into this category, and thus are named *ordered hyperuniform*. But more interestingly, there are systems that can be classified as *disordered hyperuniform*: while isotropic, with no long-range order, they feature the suppression of density fluctuations at large scales. Thus, *disordered hyperuniformity* represents a "hidden order", one that we must uncover through the characterization of density fluctuations of the system in question (see Figure 1.2). This task is usually approached by direct calculation of the particle number variance in real space, or by the static structure factor, which measures density fluctuations in Fourier space. However, the difficulty lies in finding the best observable for each particular case, as it may happen that one of these quantities does not show hyperuniformity, while the other does.

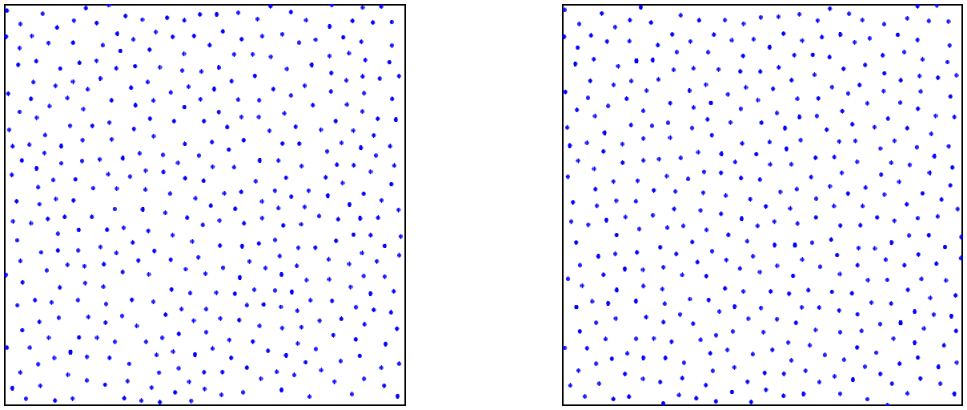

(a) (b)

Figure 1.2: Two disordered configurations, (a) nonhyperuniform and (b) hyperuniform (b). The comparison makes evident how difficult is to detect hyperuniformity by eye, and why it can be regarded as a "hidden order" [2].

1.1 Hyperuniformity in nature

Since the introduction of the concept, hyperuniformity has been identified in a variety of systems from diverse fields, and several potential applications have been theorized due to novel properties it possesses. In cosmology, the standard theories of structure formation describe the density field in the early universe as a perfectly homogeneous and isotropic distribution of matter, with the imposition of very small fluctuations, described by the so-called Harrison-Zeldovich (HZ) power spectrum. After the Cosmic Background Explorer (COBE) experiment measured for the first time the large-scale fluctuations of the temperature in the cosmic microwave background radiation, results were consistent with the predictions of HZ spectrum models. Therefore, the HZ spectra became a central pillar of standard models

of structure formation in the early universe. It was shown by Gabrielli *et al.* [3] that the distribution that reproduces the HZ behavior is in fact "superhomogeneous" (which was the term competing with "hyperuniformity" around the time of publication of their work). Understanding the physical processes that produce a hyperuniform state could be fundamental to comprehend how and why the Universe as we know it came to be, since the small density fluctuations characterized by the HZ spectra are believed to be the reason for the emergence of galaxies and other structures through a complex dynamical evolution.

Most colors present in the animal kingdom are due to pigmentation. But there are only a handful of species that can produce a blue pigment, which is the reason why this color is extremely rare. Some butterfly species have blue colored wings, but it is not pigmentary, it is a structural color: the scales in their wings are *photonic crystals* that only allow light in the blue portion of the visible spectrum to reflect. Photonic crystals are optical structures that affect the motion of photons analogously to the way a periodic potential in a semiconductor crystal affects the motion of electrons, by defining allowed and forbidden energy bands: a photonic band gap (PBG). But the PBG structure found in butterfly wings has an angular dependence, inherent to the lack of isotropy imposed by the crystalline structure. Work by Florescu *et al.* showed that Complete PBG materials (that is, with an isotropic photonic band gap) could be designed using hyperuniformity [4]. This was later experimentally proved by building a hyperuniform arrangement of air enclosing cells formed by a connected network of dielectric walls that displayed the expected complete PBG [5]. All the current applications of PBG materials, such as thin-film coatings of lenses and mirrors, photonic-crystal fiber (PCF) and security printing share the limitations of angular dependence, since they are designed as photonic crystals. A better understanding of how hyperuniformity can be generated could lead to the production of more advanced materials with a complete PBG.

Vision has the purpose of sampling light to provide an organism with information of its surroundings, allowing it to survive. According to sampling theory, the most effective way to accomplish this goal is by a perfectly regular 2D array of photoreceptors that allow to evenly sample the incoming light, in order to generate an accurate representation of the environment. Any deviation from this highly regular arrangement results in a deteriorated image. Most arthropods, like insects and crustaceans have this kind of structure in the form of compound eyes, which consist of thousands of photoreceptive units, or ommatidia, in a periodic lattice (see Figure 1.3a). Nevertheless, it has been found that the photoreceptive cells in chickens eyes are disorderly arranged in the retina, which is very surprising considering that diurnal birds have one of the most sophisticated visual systems of any vertebrate: four types of single cone cells responsible for color vision (red, green, blue and violet) and double cones involved in the detection of intensity (see Figure 1.3b). Recent research [6] showed that, not only the overall distribution of cone cells is hyperuniform, but each cell type when isolated is also hyperuniform, a phenomenon that has been termed *multihyperuniformity*. These findings suggest that a disordered hyperuniform pattern may produce a different optimal sampling arrangement, given the existence of some constraints imposed on the photoreceptors because of their interactions. Jiao *et al.* suggest that these constraints represent a compromise between the tendency of individual cell types to maximize their spatial regularity, and the counter-effect of polydisperse packing of different types of cells.

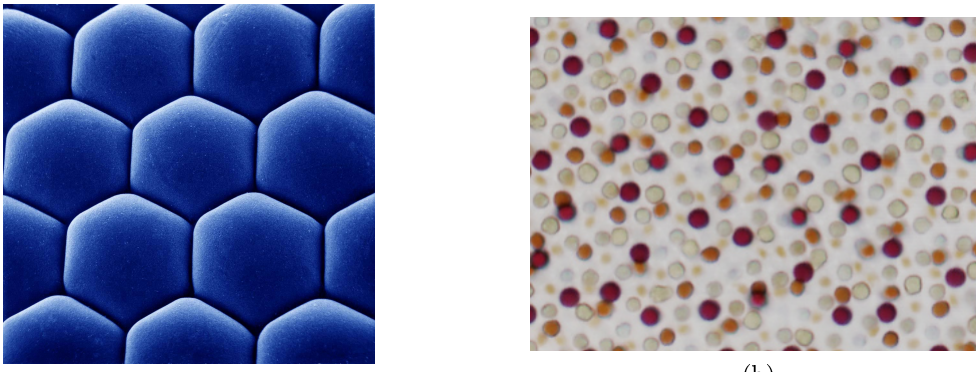

(a) (b)

Figure 1.3: Examples of hyperuniformity found in nature. (a) Ommatidia of a krill, displaying a hexagonal lattice organization. Photograph by Uwe Kils, under a CC-BY-SA-3.0 license. (b) Chicken cone cells have a multihyperuniform distribution in the retina [6].

1.2 Granular matter and hyperuniformity

Beans and condiments in our kitchens, powders in the pharmaceutical industry, landslides and other geomorphic processes, the asteroid belt in the solar system and cosmic dust clouds in space; all of these are examples of how vast, diverse and ubiquitous granular matter is. By definition, a granular material is a conglomeration of discrete, solid, macroscopic particles that interact mainly through solid contacts. Grains can have a variety of shapes and compositions, and can span over several orders of magnitude in size, but are considered to be large enough so that thermal fluctuations do not intervene in their motion. In comparison, thermal energy at room temperature (298 K) is of the order of $k_B T \sim 10^{-21}$ J, while for granular particles of mass $m \sim 10^{-6}$ kg and diameter $a \sim 10^{-3}$ m, the energy can be approximated by $mga \sim 10^{-9}$ J.

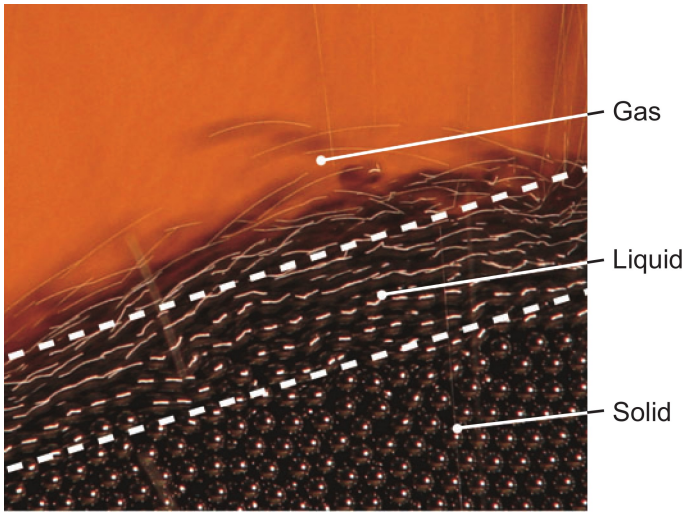

Figure 1.4: Solid, liquid, and gas flow regimes obtained by pouring steel beads on a pile [7].

Thus, when there is no energy injection, and the particles are at rest relative to each other in the presence of gravity, a granular material behaves like a solid. However, this solid lacks a uniform distribution of stress due to the inhomogeneous distribution of contacts between

grains. Instead, stress is conducted through force chains, which are networks of particles resting on one another. On the other hand, if the granular material is driven with sufficient energy so that contacts between particles become highly infrequent, it behaves like a liquid or gas (see Figure 1.4). Despite these similarities, granular media has a fundamental difference with conventional states of matter: the dissipative collisions between the grains imply the need of continuous energy injection in order to sustain a dynamical state. Therefore, they are intrinsically out of equilibrium.

Recently, hyperuniformity has been observed in a few granular systems. Random jammed sphere packings were theorized to present hyperuniformity, and have been successfully demonstrated to do so [8]. As it was mentioned before, the main difficulty lies in finding the best observable to describe the suppression of density fluctuations at large scales. In jammed packings of size-disperse spheres, the structure factor does not display the expected hyperuniform behavior, despite being observed through the particle number variance. Berthier *et al.* show that in this case, the compressibility vanishes for infinite wavelengths, and thus proves to be a more adequate quantity to describe the hyperuniform state of the system [9]. In the case of multi-phase media, the particle number variance is not well suited to quantify the fluctuations of density, since it does not account for different volume fractions of the different phases that compose the system. In this case, a more general definition of hyperuniformity must be employed, which relies on the variance of the local volume fraction [10].

Our particular case is that of a collection of hard spheres confined in a quasi-2D cell, where the lateral dimensions are much larger than the height of the cell, which is constantly fluidized through vibration. This system presents a liquid-to-solid-like phase transition where, past a critical acceleration, a fluidized liquid phase coexists with a solid, crystalline cluster. The phase transition has the peculiarity of being first or second order, depending on the height of the cell or the particle density, and has been previously characterized [11, 12, 13]. In this thesis, we present an experimental study of density fluctuations in this system, and aim to demonstrate the existance of hyperuniform states that are dinamically generated. Additionally, the analysis of diffusion in the systems grants us an insight on a possible interpretation of this phenomenon, that could lead to a better understanding on the nature of hyperuniformity.

1.3 Objectives

To summarize, the main objectives of this thesis are:

- To characterize hyperuniformity in a vibrated granular quasi-2D system that undegoes a liquid-to-solid-like phase transition.
- To study the transport of the grains, and its relation to the dynamic generation of hyperuniform states.

1.4 Outline

This thesis is organized as follows: In Chapter 2, we introduce the main quantities used to measure density fluctuations, in order to formally define the concept of hyperuniformity and

its characterization. Then, in Chapter 3, we present a brief review on diffusion, which will be useful to study the transport of grains in our system. In Chapter 4, we present the existing experimental setup, the improvements done during this thesis, and the computional tools we use to detect and track particles. In Chapter 5 we present some results from previous work in this same setup, particularly the order parameter used to characterize the phase transition present in the system. In Chapter 6, we show the results of the characterization of hyperuniformity in our particular setup, via the variance of the particle number and the static structure factor, and the corresponding discussion on which of these parameters is the best suited for this task. Through the study of diffusion in the system, we propose an explanation on how these dynamic hyperuniform states are generated in the system. Finally, in Chapter 7 we present our final remarks and an insight on the possible direction for future research on this topic.

Chapter 2

Hyperuniformity

The unusual suppression of density fluctuations at large length scales is the central characteristic of hyperuniformity. As we have mentioned before, there is no apparent visual pattern that can help us identify a hyperuniform state: we must quantify density fluctuations and verify that they are indeed suppressed for large scales. The difficulty lies in finding the best observable to accomplish this task, as it must be done for each particular case. In this chapter, we review the main tools employed to study density fluctuations, and the definition of hyperuniformity. First, in Section §2.1, we define the particle number variance and the structure factor as the quantities that allow us to measure density fluctuations in real and Fourier space, respectively, and then derive the relation between them. In Section §2.2, we give an intuitive description of the expected behavior of these quantities in a hyperuniform system, followed by a more thorough mathematical description, which will lay the foundation for the characterization of hyperuniformity in our particular experiment.

2.1 Density fluctuations in real and reciprocal space

Density fluctuations, as it is well known, contain crucial thermodynamic and structural information about many-particle systems. Hence, characterizing them is a fundamental problem of great interest for a wide variety of areas, such as physics, biology and materials science. Measurements of galaxy density fluctuations represent a powerful tool to study the large-scale structure of the Universe [14]. The quantification of density fluctuations has revealed that structures within cells have a fractal nature [15], and has been used to distinguish the spatial distribution of cancer cells from that of normal, healthy cells [16]. In granular media, density fluctuations have allowed us to explore structure and collective motion of vibrated grains [11, 12, 17]. Henceforth, we will define the main tools used to describe density fluctuations in a system.

2.1.1 Structure factor and total correlation function

Let us consider a system of N particles in a volume V in $\mathbb{R}^n$, with configuration $\mathbf{r}^N = \mathbf{r}_1, \mathbf{r}_2, \ldots, \mathbf{r}_N$. The local number density at position $\mathbf{x}$ is given by

$$\rho(\mathbf{x}) = \sum_{j=1}^{N} \delta(\mathbf{x} - \mathbf{r}_j)\,, \tag{2.1.1}$$

where $\delta(\mathbf{x})$ is the Dirac delta function. We can define the probability density $P\big(\mathbf{r}^N\big)$, such that $P\big(\mathbf{r}^N\big)\,\mathrm{d}\mathbf{r}^N$ gives the probability of finding partice 1 in volume element $\mathrm{d}\mathbf{r}_1$ about $\mathbf{r}_1$, particle 2 in volume element $\mathrm{d}\mathbf{r}_2$ about $\mathbf{r}_2$, and so on. Thus, $P\big(\mathbf{r}^N\big)$ normalizes to unity and $\mathrm{d}\mathbf{r}^N \equiv \mathrm{d}\mathbf{r}_1\,\mathrm{d}\mathbf{r}_2 \cdots \mathrm{d}\mathbf{r}_N$ represents the $(N \times n)$-dimensional volume element. The ensemble average of any function $f\big(\mathbf{r}^N\big)$ is given by

$$\big\langle f\big(\mathbf{r}^N\big)\big\rangle = \int_V \cdots \int_V f\big(\mathbf{r}^N\big) P\big(\mathbf{r}^N\big)\,\mathrm{d}\mathbf{r}^N\ . \tag{2.1.2}$$

Given that complete statistical information is usually unavailable, it is convenient to introduce the reduced generic density function $p_j(\mathbf{r}^j)$ $(j < N)$, defined as

$$p_j\big(\mathbf{r}^j\big) = \frac{N!}{(N-j)!} \int_V \cdots \int_V P_N\big(\mathbf{r}^N\big)\,\mathrm{d}\mathbf{r}^{N-j}\ , \tag{2.1.3}$$

where $\mathrm{d}\mathbf{r}^{N-j} \equiv \mathrm{d}\mathbf{r}_{j+1}\,\mathbf{r}_{j+1} \cdots \mathbf{r}_N$. In words, $p_j(\mathbf{r}^j)\,\mathrm{d}\mathbf{r}^j$ is proportional to the probability of finding *any* $j \leq N$ particles with configuration $\mathbf{r}^j$ in volume element $\mathrm{d}\mathbf{r}^j$. For statistically homogeneous media, $p_j(\mathbf{r}^j)$ is translationally invariant so it must depend only on the relative displacements, say with respect to $\mathbf{r}_1$:

$$p_j\big(\mathbf{r}^j\big) = p_j(\mathbf{r}_{12}, \mathbf{r}_{13}, \ldots, \mathbf{r}_{1j})\,, \tag{2.1.4}$$

where $\mathbf{r}_{ij} = \mathbf{r}_j - \mathbf{r}_i$.

Note that the definition in equation (2.1.3) implies that

$$\int_V p_j\big(\mathbf{r}^j\big)\,\mathrm{d}\mathbf{r}^j = \frac{N!}{(N-j)!}\,, \tag{2.1.5}$$

where $\mathrm{d}\mathbf{r}^j = \mathrm{d}\mathbf{r}_1\,\mathrm{d}\mathbf{r}_2 \cdots \mathrm{d}\mathbf{r}_j$. In particular, for the one-particle function $p_1(\mathbf{r}_1)$,

$$\int_V p_1(\mathbf{r}_1)\,\mathrm{d}\mathbf{r}_1 = \frac{N!}{(N-1)!} = N\,, \tag{2.1.6}$$

and therefore, $p_1(\mathbf{r}_1)$ is just equal to the constant number density of particles ρ_0, that is,

$$p_1(\mathbf{r}_1) = \rho_0 \equiv \lim_{N,V\to\infty} \frac{N}{V}\,, \tag{2.1.7}$$

where we have taken the thermodynamic limit. Additionally, if we calculate the average of the product of two Dirac deltas, we obtain

$$\left\langle \sum_{i=1}^{N} \sum_{j\neq i} \delta(\mathbf{x} - \mathbf{r}_i)\delta(\mathbf{x}' - \mathbf{r}_j) \right\rangle = \int_V \sum_{i=1}^{N} \sum_{j\neq i} \delta(\mathbf{x} - \mathbf{r}_i)\delta(\mathbf{x}' - \mathbf{r}_j) P\big(\mathbf{r}^N\big)\,\mathrm{d}\mathbf{r}^N \tag{2.1.8}$$

$$= \int_V N(N-1) P\big(\mathbf{r}^N\big)\,\mathrm{d}\mathbf{r}^{N-2} \tag{2.1.9}$$

$$= \frac{N!}{(N-1)!} \int_V P\big(\mathbf{r}^N\big)\,\mathrm{d}\mathbf{r}^{N-2}\ , \tag{2.1.10}$$

which is just $p_2(\mathbf{x}, \mathbf{x}')$. Therefore, we have the alternative expression,

$$p_2(\mathbf{r}) = \left\langle \sum_{i=1}^{N} \sum_{j \neq i} \delta(\mathbf{x} - \mathbf{r}_i)\delta(\mathbf{x}' - \mathbf{r}_j) \right\rangle , \tag{2.1.11}$$

where $\mathbf{r} \equiv \mathbf{x} - \mathbf{x}'$, assuming translational invariance. Now, we define the *pair correlation function*,

$$g_2(\mathbf{r}) = \frac{p_2(\mathbf{r})}{\rho_0^2} . \tag{2.1.12}$$

In systems without long-range order and in which the particles are mutually far from one another, $p_2(\mathbf{r}) \to \rho_0^2$ and therefore, $g_2(\mathbf{r}^2) \to 1$. Thus, deviation of g_2 from unity provides a measure of the degree of spatial correlation between the particles, with unity corresponding to no spatial correlation at all. On the other hand, the *total correlation function,*

$$h(\mathbf{r}) = g_2(\mathbf{r}) - 1 , \tag{2.1.13}$$

is defined in such a way that is zero when there are no spatial correlations in the system.

The *static structure factor* measures density fluctuations in the reciprocal space. The Fourier transform of an absolutely integrable function $f(\mathbf{x})$ in n dimensions is given by

$$\hat{f}(\mathbf{k}) = \int f(\mathbf{x}) e^{-\mathrm{i}\mathbf{k}\cdot\mathbf{x}} , \tag{2.1.14}$$

and the associated inverse transform is

$$f(\mathbf{x}) = \frac{1}{(2\pi)^n} \int \hat{f}(\mathbf{k}) e^{\mathrm{i}\mathbf{k}\cdot\mathbf{x}} . \tag{2.1.15}$$

Accordingly, the structure factor is defined as

$$S(\mathbf{k}) = \frac{\left\langle |\hat{\rho}(\mathbf{k})|^2 \right\rangle}{N} , \tag{2.1.16}$$

where $\hat{\rho}(\mathbf{k})$ is the Fourier transform of the density,

$$\hat{\rho}(\mathbf{k}) = \int \rho(\mathbf{x}) e^{-\mathrm{i}\mathbf{k}\cdot\mathbf{x}} \, \mathrm{d}\mathbf{x} \tag{2.1.17}$$

$$= \int \sum_{j=1}^{N} \delta(\mathbf{x} - \mathbf{r}_j) e^{-\mathrm{i}\mathbf{k}\cdot\mathbf{x}} \, \mathrm{d}\mathbf{x} \tag{2.1.18}$$

$$= \sum_{j=1}^{N} e^{-\mathrm{i}\mathbf{k}\cdot\mathbf{r}_j} . \tag{2.1.19}$$

In condensed matter, the structure factor is used to describe the scattering of incident radiation on materials. For regular lattices, $S(\mathbf{k})$ exhibits sharp peaks at certain wavelengths that are related to the structure of the crystal. X-ray crystallography allows us to identify the crystalline structure of a material by measuring the intensity of X-rays scattered in different directions, which is related to the structure factor [18]. In liquids, the lack of long-range order

implies that there are no sharp peaks in $S(\mathbf{k})$, although it can display a certain degree of short to medium range order depending on the strength of the interaction between particles or their density [19]. X-ray diffraction can be used to measure the structure factor directly, and it can also be calculated for hard-sphere models with different types of interaction potentials (See Figure 2.1).

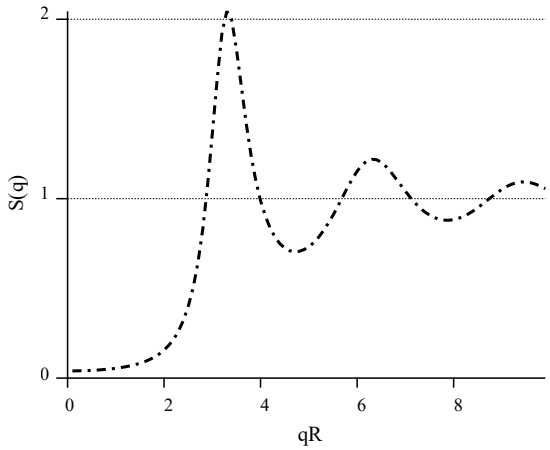

Figure 2.1: Calculated structure factor of a hard-sphere fluid, with wavenumber q and particle radius R. The existance of short or medium range order produces the peak observed. Figure adapted from image by Dcconsta at Wikimedia Commons, under a CC-BY-SA-3.0 license.

The structure factor is also related to the fourier transform of the total correlation function. From the definition, we obtain

$$S(\mathbf{k}) = \frac{1}{N}\left\langle \hat{\rho}(\mathbf{k})\hat{\rho}^{\dagger}(\mathbf{k})\right\rangle \tag{2.1.20}$$

$$= \frac{1}{N}\left\langle \sum_{i=1}^{N}\sum_{j=1}^{N} e^{-\mathrm{i}\mathbf{k}\cdot(\mathbf{r}_i-\mathbf{r}_j)}\right\rangle \tag{2.1.21}$$

$$= 1 + \frac{1}{N}\left\langle \sum_{i=1}^{N}\sum_{j\neq i}^{N} e^{-\mathrm{i}\mathbf{k}\cdot(\mathbf{r}_i-\mathbf{r}_j)}\right\rangle \tag{2.1.22}$$

$$= 1 + \frac{1}{N}\left\langle \sum_{i=1}^{N}\sum_{j\neq i}^{N} \int\int e^{-\mathrm{i}\mathbf{k}\cdot(\mathbf{x}-\mathbf{x}')}\delta(\mathbf{x}-\mathbf{r}_i)\delta(\mathbf{x}'-\mathbf{r}_j)\,\mathrm{d}\mathbf{x}\,\mathrm{d}\mathbf{x}'\right\rangle \tag{2.1.23}$$

$$= 1 + \frac{1}{N}\int\int e^{-\mathrm{i}\mathbf{k}\cdot(\mathbf{x}-\mathbf{x}')}\left\langle \sum_{i=1}^{N}\sum_{j\neq i}^{N} \delta(\mathbf{x}-\mathbf{r}_i)\delta(\mathbf{x}'-\mathbf{r}_j)\right\rangle \mathrm{d}\mathbf{x}\,\mathrm{d}\mathbf{x}' \tag{2.1.24}$$

$$= 1 + \frac{1}{N}\int\int e^{-\mathrm{i}\mathbf{k}\cdot(\mathbf{x}-\mathbf{x}')} p_2(\mathbf{x}-\mathbf{x}')\,\mathrm{d}\mathbf{x}\,\mathrm{d}\mathbf{x}'\ , \tag{2.1.25}$$

where we have used equation (2.1.11). Exploiting our assumption of translational invariance to integrate over $\mathbf{x}'$ and recalling that $\mathbf{r} = \mathbf{x} - \mathbf{x}'$, it yields

$$S(\mathbf{k}) = 1 + \frac{1}{\rho_0}\int e^{-\mathrm{i}\mathbf{k}\cdot\mathbf{r}} p_2(\mathbf{r})\,\mathrm{d}\mathbf{r} \tag{2.1.26}$$

$$= 1 + \frac{1}{\rho_0}\int e^{-\mathrm{i}\mathbf{k}\cdot\mathbf{r}} \rho_0^2 g_2(\mathbf{r})\,\mathrm{d}\mathbf{r} \tag{2.1.27}$$

$$= 1 + \rho_0 \int e^{-\mathrm{i}\mathbf{k}\cdot\mathbf{r}} g_2(\mathbf{r})\,\mathrm{d}\mathbf{r}\ . \tag{2.1.28}$$

The last integral ressembles a Fourier transform of the pair correlation function. However, $g_2(\mathbf{r})$ is not absolutely integrable, as $\lim_{|r|\to\infty} g_2(\mathbf{r}) = 1$. To bypass this, we extract the singularity from the integral,

$$S(\mathbf{k}) = 1 + \rho_0 \int e^{-\mathrm{i}\mathbf{k}\cdot\mathbf{r}} (g_2(\mathbf{r}) - 1 + 1)\,\mathrm{d}\mathbf{r} \tag{2.1.29}$$

$$= 1 + \rho_0 \int e^{-\mathrm{i}\mathbf{k}\cdot\mathbf{r}} (g_2(\mathbf{r}) - 1)\,\mathrm{d}\mathbf{r} + \rho_0 \int e^{-\mathrm{i}\mathbf{k}\cdot\mathbf{r}}\,\mathrm{d}\mathbf{r}\ . \tag{2.1.30}$$

But the parenthesis is just $h(\mathbf{r})$, and the last term is proportional to a Dirac delta in Fourier space. Hence,

$$S(\mathbf{k}) = 1 + \rho_0 \int e^{-\mathrm{i}\mathbf{k}\cdot\mathbf{r}} h(\mathbf{r})\,\mathrm{d}\mathbf{r} + (2\pi)^n \rho_0 \delta(k) \tag{2.1.31}$$

$$= 1 + \rho_0 \hat{h}(\mathbf{k}) + (2\pi)^n \rho_0 \delta(k)\,, \tag{2.1.32}$$

remarking that the Fourier transform of the total correlation function, $\hat{h}(\mathbf{k})$, is well defined. This result implies that the structure factor has a singularity for $\mathbf{k} = \mathbf{0}$. Experimentally, this corresponds to *forward scattering*, that is, radiation that passes through the sample unscattered. Henceforth, we will ignore this contribution in the structure factor, and therefore,

$$S(\mathbf{k}) = 1 + \rho_0 \hat{h}(\mathbf{k})\,. \tag{2.1.33}$$

2.1.2 Particle number variance

The particle number variance measures density fluctuations in real space. We will consider an observation window Ω whose geometry is characterized by parameters $\mathbf{R}$. For a spherical window, $\mathbf{R}$ would represent its radius, while for a square window, its side. The particle number variance in an observation window Ω is defined as

$$\sigma_N^2(R) = \left\langle N(R)^2 \right\rangle - \left\langle N(R) \right\rangle^2\ , \tag{2.1.34}$$

where $\langle N(\mathbf{R})\rangle$ is the average number of particles inside Ω. Let us introduce the window indicator function

$$v(\mathbf{x} - \mathbf{x}_0) = \begin{cases} 1\,, & \mathbf{x} \in \Omega \\ 0\,, & \mathbf{x} \notin \Omega\,, \end{cases} \tag{2.1.35}$$

for a window with centroid $\mathbf{x}_0$. The number of particles contained within the window Ω centered at $\mathbf{x}_0$, which we will denote $N_\Omega(\mathbf{x}_0;\mathbf{R})$, is given by

$$N_\Omega(\mathbf{x}_0;\mathbf{R}) = \int_V \rho(\mathbf{x})\upsilon(\mathbf{x}-\mathbf{x}_0;\mathbf{R})\,\mathrm{d}\mathbf{x} \tag{2.1.36}$$

$$= \sum_{j=1}^{N} \int_V \delta(\mathbf{x}-\mathbf{r}_j)\upsilon(\mathbf{x}-\mathbf{x}_0;\mathbf{R})\,\mathrm{d}\mathbf{x} \tag{2.1.37}$$

$$= \sum_{j=1}^{N} \upsilon(\mathbf{r}_j-\mathbf{x}_0;\mathbf{R})\,. \tag{2.1.38}$$

Therefore, the average number of particles within an observation window Ω can be calculated as

$$\langle N(\mathbf{R})\rangle = \int_V N_\Omega(\mathbf{x}_0;\mathbf{R})P\big(\mathbf{r}^N\big)\,\mathrm{d}\mathbf{r}^N \tag{2.1.39}$$

$$= \int_V \sum_{j=1}^{N} \upsilon(\mathbf{r}_j-\mathbf{x}_0;\mathbf{R})P\big(\mathbf{r}^N\big)\,\mathrm{d}\mathbf{r}^N \tag{2.1.40}$$

$$= \int_V N\upsilon(\mathbf{r}_1-\mathbf{x}_0;\mathbf{R})P\big(\mathbf{r}^N\big)\,\mathrm{d}\mathbf{r}^N\ , \tag{2.1.41}$$

where we have replaced the sum by N times a single term, given that we are integrating over every possible configuration of the system. Now, we will separate the differential, to make use of equation (2.1.3),

$$\langle N(\mathbf{R})\rangle = \int_V N\upsilon(\mathbf{r}_1-\mathbf{x}_0;\mathbf{R})\left(\int_V P\big(\mathbf{r}^N\big)\,\mathrm{d}\mathbf{r}^{N-1}\right)\mathrm{d}\mathbf{r}_1 \tag{2.1.42}$$

$$= \int_V N\upsilon(\mathbf{r}_1-\mathbf{x}_0;\mathbf{R})\left(\frac{(N-1)!}{N!}p_1(\mathbf{r}_1)\right)\mathrm{d}\mathbf{r}_1 \tag{2.1.43}$$

$$= \int_V \upsilon(\mathbf{r}_1-\mathbf{x}_0;\mathbf{R})p_1(\mathbf{r}_1)\,\mathrm{d}\mathbf{r}_1\ . \tag{2.1.44}$$

Here, we recall that $p_1(\mathbf{r}_1)=\rho_0$, thus yielding

$$\langle N(\mathbf{R})\rangle = \rho_0 \int_V \upsilon(\mathbf{r}_1-\mathbf{x}_0;\mathbf{R})\,\mathrm{d}\mathbf{r}_1 \tag{2.1.45}$$

$$= \rho_0 \int_V \upsilon(\mathbf{r}-\mathbf{x}_0;\mathbf{R})\,\mathrm{d}\mathbf{r}\ , \tag{2.1.46}$$

where we have dropped the subindex for $\mathbf{r}$. Additionally, the translational invariance implies that the average cannot depend on the position of the window, $\mathbf{x}_0$, thus

$$\langle N(\mathbf{R})\rangle = \rho_0 \int_V \upsilon(\mathbf{r};\mathbf{R})\,\mathrm{d}\mathbf{r}\ . \tag{2.1.47}$$

But now the integral is just the volume of the window Ω, therefore

$$\langle N(\mathbf{R})\rangle = \rho_0 V_1(\mathbf{R})\,, \tag{2.1.48}$$

where we have defined the volume as

$$V_1(\mathbf{R}) = \int_{\mathbb{R}^n} \upsilon(\mathbf{r};\mathbf{R})\,\mathrm{d}\mathbf{r}\ . \tag{2.1.49}$$

Similarly, we can calculate the ensemble average of the number of particles inside Ω squared

$$\left\langle N^2(\mathbf{R})\right\rangle = \int_V N_\Omega^2(\mathbf{x}_0;\mathbf{R}) P\big(\mathbf{r}^N\big)\,\mathrm{d}\mathbf{r}^N \tag{2.1.50}$$

$$= \int_V \left(\sum_{i=1}^N \upsilon(\mathbf{r}_i - \mathbf{x}_0;\mathbf{R})\right)^2 P\big(\mathbf{r}^N\big)\,\mathrm{d}\mathbf{r}^N\ . \tag{2.1.51}$$

If we expand the square of the sum, it allows us to split the integral

$$\begin{aligned}\left\langle N^2(\mathbf{R})\right\rangle = \int_V \Bigg(&\sum_{i=1}^N \upsilon^2(\mathbf{r}_i - \mathbf{x}_0;\mathbf{R}) \\ &+2\sum_{i=1}^N\sum_{j\neq i} \upsilon(\mathbf{r}_i - \mathbf{x}_0;\mathbf{R})\upsilon(\mathbf{r}_j - \mathbf{x}_0;\mathbf{R})\Bigg) P\big(\mathbf{r}^N\big)\,\mathrm{d}\mathbf{r}^N\end{aligned} \tag{2.1.52}$$

$$\begin{aligned}= &\int_V \sum_{i=1}^N \upsilon^2(\mathbf{r}_i - \mathbf{x}_0;\mathbf{R}) P\big(\mathbf{r}^N\big)\,\mathrm{d}\mathbf{r}^N \\ &+ 2\int_V \sum_{i=1}^N\sum_{j\neq i} \upsilon(\mathbf{r}_i - \mathbf{x}_0;\mathbf{R})\upsilon(\mathbf{r}_j - \mathbf{x}_0;\mathbf{R}) P\big(\mathbf{r}^N\big)\,\mathrm{d}\mathbf{r}^N\ .\end{aligned} \tag{2.1.53}$$

Now, we note that $\upsilon^2(\mathbf{r}_j - \mathbf{x}_0;\mathbf{R}) = \upsilon(\mathbf{r}_j - \mathbf{x}_0;\mathbf{R})$, and thus

$$\begin{aligned}\left\langle N^2(\mathbf{R})\right\rangle = &\int_V \sum_{j=1}^N \upsilon(\mathbf{r}_j - \mathbf{x}_0;\mathbf{R}) P\big(\mathbf{r}^N\big)\,\mathrm{d}\mathbf{r}^N \\ &+ 2\int_V \sum_{i=1}^N\sum_{j\neq i} \upsilon(\mathbf{r}_i - \mathbf{x}_0;\mathbf{R})\upsilon(\mathbf{r}_j - \mathbf{x}_0;\mathbf{R}) P\big(\mathbf{r}^N\big)\,\mathrm{d}\mathbf{r}^N\ .\end{aligned} \tag{2.1.54}$$

But the first integral is just $\langle N(\mathbf{R})\rangle$. As for the second integral, we replace the sum of pairs by $N(N-1)/2$ (since the contribution of any particle pair is identical) yielding

$$\left\langle N^2(\mathbf{R})\right\rangle = \langle N(\mathbf{R})\rangle + 2\int_V \frac{N(N-1)}{2}\upsilon(\mathbf{r}_1 - \mathbf{x}_0;\mathbf{R})\upsilon(\mathbf{r}_2 - \mathbf{x}_0;\mathbf{R}) P\big(\mathbf{r}^N\big)\,\mathrm{d}\mathbf{r}^N \tag{2.1.55}$$

$$= \langle N(\mathbf{R})\rangle + \int_V N(N-1)\upsilon(\mathbf{r}_1 - \mathbf{x}_0;\mathbf{R})\upsilon(\mathbf{r}_2 - \mathbf{x}_0;\mathbf{R}) P\big(\mathbf{r}^N\big)\,\mathrm{d}\mathbf{r}^N\ . \tag{2.1.56}$$

Now, we will separate the differential again, to make use of equation (2.1.3)

$$\begin{aligned}\left\langle N^2(\mathbf{R})\right\rangle = &\langle N(\mathbf{R})\rangle \\ &+ \int_V N(N-1)\upsilon(\mathbf{r}_1 - \mathbf{x}_0;\mathbf{R})\upsilon(\mathbf{r}_2 - \mathbf{x}_0;\mathbf{R})\left(\int_V P\big(\mathbf{r}^N\big)\,\mathrm{d}\mathbf{r}^{N-2}\right)\mathrm{d}\mathbf{r}_1\,\mathrm{d}\mathbf{r}_2\end{aligned} \tag{2.1.57}$$

$$\begin{aligned}= &\langle N(\mathbf{R})\rangle \\ &+ \int_V N(N-1)\upsilon(\mathbf{r}_1 - \mathbf{x}_0;\mathbf{R})\upsilon(\mathbf{r}_2 - \mathbf{x}_0;\mathbf{R})\left(\frac{(N-2)!}{N!}p_2(\mathbf{r}_1,\mathbf{r}_2)\right)\mathrm{d}\mathbf{r}_1\,\mathrm{d}\mathbf{r}_2\ ,\end{aligned} \tag{2.1.58}$$

which finally yields

$$\left\langle N^2(\mathbf{R})\right\rangle = \langle N(\mathbf{R})\rangle + \int_V \upsilon(\mathbf{r}_1-\mathbf{x}_0;\mathbf{R})\upsilon(\mathbf{r}_2-\mathbf{x}_0;\mathbf{R})p_2(\mathbf{r}_1,\mathbf{r}_2)\,\mathrm{d}\mathbf{r}_1\,\mathrm{d}\mathbf{r}_2\ . \tag{2.1.59}$$

Now we use equation (2.1.44) to calculate the average of the number of particles squared as

$$\langle N(\mathbf{R})\rangle^2 = \int_V \upsilon(\mathbf{r}_1-\mathbf{x}_0;\mathbf{R})\upsilon(\mathbf{r}_2-\mathbf{x}_0;\mathbf{R})p_1(\mathbf{r}_1)p_1(\mathbf{r}_2)\,\mathrm{d}\mathbf{r}_1\,\mathrm{d}\mathbf{r}_2 \tag{2.1.60}$$

$$= \int_V \upsilon(\mathbf{r}_1-\mathbf{x}_0;\mathbf{R})\upsilon(\mathbf{r}_2-\mathbf{x}_0;\mathbf{R})\rho_0^2\,\mathrm{d}\mathbf{r}_1\,\mathrm{d}\mathbf{r}_2\ , \tag{2.1.61}$$

where we have used that $p_1(\mathbf{r}_1) = p_1(\mathbf{r}_2) = \rho_0$.

Replacing equations (2.1.59) and (2.1.61) in the definition of the particle number variance (2.1.34), we obtain

$$\sigma_N^2 = \langle N(\mathbf{R})\rangle + \int_V \big(p_2(\mathbf{r}_1,\mathbf{r}_2)-\rho_0^2\big)\upsilon(\mathbf{r}_1-\mathbf{x}_0;\mathbf{R})\upsilon(\mathbf{r}_2-\mathbf{x}_0;\mathbf{R})\,\mathrm{d}\mathbf{r}_1\,\mathrm{d}\mathbf{r}_2 \tag{2.1.62}$$

$$= \langle N(\mathbf{R})\rangle\left[1+\frac{1}{\langle N(\mathbf{R})\rangle}\int_V \big(p_2(\mathbf{r}_1,\mathbf{r}_2)-\rho_0^2\big)\upsilon(\mathbf{r}_1-\mathbf{x}_0;\mathbf{R})\upsilon(\mathbf{r}_2-\mathbf{x}_0;\mathbf{R})\,\mathrm{d}\mathbf{r}_1\,\mathrm{d}\mathbf{r}_2\right] \tag{2.1.63}$$

Now we recall equation (2.1.48), and factor ρ_0^2 out of the integral, which yields

$$\sigma_N^2 = \langle N(\mathbf{R})\rangle\left[1+\frac{1}{\rho_0 V_1(\mathbf{R})}\rho_0^2\int_V\left(\frac{p_2(\mathbf{r}_1,\mathbf{r}_2)}{\rho_0^2}-1\right)\upsilon(\mathbf{r}_1-\mathbf{x}_0;\mathbf{R})\upsilon(\mathbf{r}_2-\mathbf{x}_0;\mathbf{R})\,\mathrm{d}\mathbf{r}_1\,\mathrm{d}\mathbf{r}_2\right] \tag{2.1.64}$$

$$= \langle N(\mathbf{R})\rangle\left[1+\rho_0\int_V\left(\frac{p_2(\mathbf{r}_1,\mathbf{r}_2)}{\rho_0^2}-1\right)\frac{\upsilon(\mathbf{r}_1-\mathbf{x}_0;\mathbf{R})\upsilon(\mathbf{r}_2-\mathbf{x}_0;\mathbf{R})}{V_1(\mathbf{R})}\,\mathrm{d}\mathbf{r}_1\,\mathrm{d}\mathbf{r}_2\right] \tag{2.1.65}$$

$$= \langle N(\mathbf{R})\rangle\left[1+\rho_0\int_V\left(\frac{p_2(\mathbf{r}_{12})}{\rho_0^2}-1\right)\frac{\upsilon(\mathbf{r}_1-\mathbf{x}_0;\mathbf{R})\upsilon(\mathbf{r}_2-\mathbf{x}_0;\mathbf{R})}{V_1(\mathbf{R})}\,\mathrm{d}\mathbf{r}_1\,\mathrm{d}\mathbf{r}_2\right], \tag{2.1.66}$$

where, in the last line, we have invoked translational invariance once again. Defining the intersection volume of two windows (with the same orientations)

$$V_2^{int}(\mathbf{r};\mathbf{R}) \equiv \int_{\mathbb{R}^n} \upsilon(\mathbf{r}_1-\mathbf{x}_0;\mathbf{R})\upsilon(\mathbf{r}_2-\mathbf{x}_0;\mathbf{R})\,\mathrm{d}\mathbf{x}_0 \tag{2.1.67}$$

$$= \int_{\mathbb{R}^n} \upsilon(\mathbf{x}_0;\mathbf{R})\upsilon(\mathbf{x}_0+\mathbf{r};\mathbf{R})\,\mathrm{d}\mathbf{x}_0\ , \tag{2.1.68}$$

where $\mathbf{r} \equiv \mathbf{r}_{12}$ is the distance between the centroids of the two windows, and noticing that the quantity inside the parenthesis is just the total correlation function, $h(\mathbf{r})$, we can rewrite equation (2.1.66) as

$$\sigma_N^2 = \langle N(\mathbf{R})\rangle\left[1+\rho_0\int_{\mathbb{R}^n} h(\mathbf{r})\frac{V_2^{int}(\mathbf{r};\mathbf{R})}{V_1(\mathbf{R})}\,\mathrm{d}\mathbf{r}\right] \tag{2.1.69}$$

$$= \langle N(\mathbf{R})\rangle\left[1+\rho_0\int_{\mathbb{R}^n} h(\mathbf{r})\Lambda(\mathbf{r};\mathbf{R})\,\mathrm{d}\mathbf{r}\right], \tag{2.1.70}$$

where

$$\Lambda(\mathbf{r};\mathbf{R}) \equiv \frac{V_2^{int}(\mathbf{r};\mathbf{R})}{V_1(\mathbf{R})} \tag{2.1.71}$$

is the scaled intersection volume.

Plancherel's theorem in Fourier analysis states that the inner product of complex functions, f and g, is related to the inner product of their Fourier transforms, $\hat{f}$ and $\hat{g}$, as

$$\int f \cdot g^{\dagger}\, \mathrm{d}\mathbf{r} = \frac{1}{(2\pi)^n} \int \hat{f} \cdot \hat{g}^{\dagger}\, \mathrm{d}\mathbf{k}\ . \tag{2.1.72}$$

Thus, we can express equation (2.1.70) in terms of the Fourier transforms of $h(\mathbf{r})$ and $\Lambda(\mathbf{r};\mathbf{R})$:

$$\sigma_N^2 = \langle N(\mathbf{R})\rangle \left[1 + \frac{\rho_0}{(2\pi)^n} \int \hat{h}(\mathbf{k})\hat{\Lambda}(\mathbf{k};\mathbf{R})\, \mathrm{d}\mathbf{k}\right], \tag{2.1.73}$$

where

$$\hat{\Lambda}(\mathbf{k};\mathbf{R}) = \frac{\hat{V}_2^{int}(\mathbf{k};\mathbf{R})}{V_1(\mathbf{R})}\,. \tag{2.1.74}$$

But the Fourier transform of V_2^{int} corresponds to

$$\hat{V}_2^{int}(\mathbf{k};\mathbf{R}) = \hat{v}^2(\mathbf{k},\mathbf{R})\,, \tag{2.1.75}$$

where $\hat{v}(\mathbf{k},\mathbf{R})$ is the Fourier transform of the window indicator function. Then,

$$\hat{\Lambda}(\mathbf{k};\mathbf{R}) = \frac{\hat{v}^2(\mathbf{k},\mathbf{R})}{V_1(\mathbf{R})}\,. \tag{2.1.76}$$

Turning back to the particle number variance

$$\sigma_N^2 = \langle N(\mathbf{R})\rangle \left[1 + \frac{1}{(2\pi)^n} \int \rho_0 \hat{h}(\mathbf{k})\hat{\Lambda}(\mathbf{k};\mathbf{R})\, \mathrm{d}\mathbf{k}\right], \tag{2.1.77}$$

using equation (2.1.33), we rewrite

$$\sigma_N^2 = \langle N(\mathbf{R})\rangle \left[1 + \frac{1}{(2\pi)^n} \int (S(\mathbf{k}) - 1)\hat{\Lambda}(\mathbf{k};\mathbf{R})\, \mathrm{d}\mathbf{k}\right], \tag{2.1.78}$$

and splitting the integral, we obtain

$$\sigma_N^2 = \langle N(\mathbf{R})\rangle \left[1 + \frac{1}{(2\pi)^n} \int S(\mathbf{k})\hat{\Lambda}(\mathbf{k};\mathbf{R})\, \mathrm{d}\mathbf{k} - \frac{1}{(2\pi)^n} \int \hat{\Lambda}(\mathbf{k};\mathbf{R})\, \mathrm{d}\mathbf{k}\right]. \tag{2.1.79}$$

However, with equation (2.1.76) and Plancherel's theorem, the second integral yields

$$\begin{aligned}
\frac{1}{(2\pi)^n} \int \hat{\Lambda}(\mathbf{r};\mathbf{R})\, \mathrm{d}\mathbf{r} =& \frac{1}{(2\pi)^n} \int \frac{\hat{v}^2(\mathbf{k},\mathbf{R})}{V_1(\mathbf{R})}\, \mathrm{d}\mathbf{k} && (2.1.80)\\
=& \frac{1}{V_1(\mathbf{R})} \frac{1}{(2\pi)^n} \int \hat{v}^2(\mathbf{k},\mathbf{R})\, \mathrm{d}\mathbf{k} && (2.1.81)\\
=& \frac{1}{V_1(\mathbf{R})} \int v^2(\mathbf{r},\mathbf{R})\, \mathrm{d}\mathbf{r} && (2.1.82)\\
=& \frac{1}{V_1(\mathbf{R})} \int v(\mathbf{r},\mathbf{R})\, \mathrm{d}\mathbf{r}\ . && (2.1.83)\\
=& 1\,, && (2.1.84)
\end{aligned}$$

where we have recalled equation (2.1.49). Replacing this result in equation (2.1.79), we finally obtain

$$\sigma_N^2(\mathbf{R}) = \langle N(\mathbf{R}) \rangle \frac{1}{(2\pi)^n} \int S(\mathbf{k}) \hat{\Lambda}(\mathbf{k}; \mathbf{R}) \, \mathrm{d}\mathbf{k} \, . \tag{2.1.85}$$

This last result reveals the expected equivalence of measuring density fluctuations in real space, through the particle number variance, or Fourier space, through the structure factor.

2.2 Characterization of hyperuniformity

We have stablished the particle number variance and structure factor as means to quantify density fluctuations in real and reciprocal space, respectively, and the equivalence of both descriptions. As we have previously stated, hyperuniform systems are characterized by the suppression of density fluctuations on large scales. In this section we will give a hand-waving explanation of what this means in terms of σ_N^2 and $S(\mathbf{k})$, followed by a more thorough mathematical description.

2.2.1 Hyperuniformity

Let us consider a system of particles distributed arbitrarily in 2D, and a circular window of radius R which encloses a part of this system. The average number of particles confined by the window should be proportional to its area (as we found in equation (2.1.48)), but the behavior of the particle number variance should depend on the particular distribution. Figure 2.2a shows a pictoric representation of a disordered distribution of particles in 2D. We observe that the variation in the number of particles enclosed by the circles grows with the area, since the density of particles varies within the circle. Therefore, the particle number variance should be proportional to the area of the window.

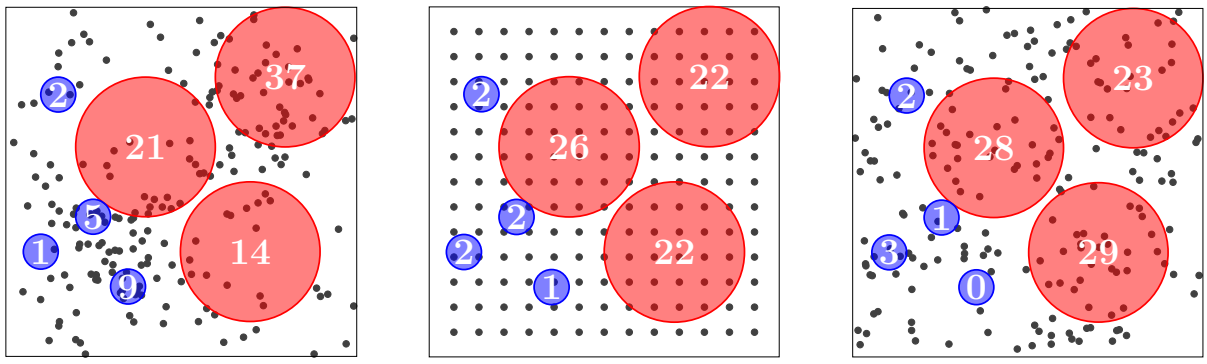

(a) (b) (c)

Figure 2.2: Schematic of the number of particles enclosed by circles for a disordered non-hyperuniform system (a), a regular lattice (b) and a disordered hyperuniform system (c). The variation in the number of particles inside small circles for a hyperuniform state is similar to that of an arbitrary disordered system, but for large circles this variation decays, like in the regular lattice.

Now we consider a regular lattice in 2D, as in Figure 2.2b. Observe that for small circles, there is no variation on the number of particles. As we increase the circle radius, the number of particles varies more, but not as much as for the disordered distribution in Figure 2.2a. In fact, variation only occurs at the boundary, because the regularity of the lattice makes the number of particles in the bulk virtually constant for same-size circles. Thus, for a regular lattice, the variance is proportional to the perimeter of the circular window.

Figure 2.2c shows a disordered hyperuniform distribution in 2D. We observe that the variation of the number of particles for small circles is similar to the disordered case in Figure 2.2a, but for large circles, it reproduces the behavior of regular lattices. This large-scale decay of the particle correlations can be used to characterize hyperuniformity: any 2D system in which the particle number variance grows slower than the area of an observation window, in the infinite window-size limit, is hyperuniform [1]. For a hyperuniform system of arbitrary dimension n,

$$\lim_{\mathbf{R}\to\infty} \frac{\sigma_N^2(\mathbf{R})}{V_1(\mathbf{R})} = 0\,, \tag{2.2.1}$$

where $\mathbf{R} \to \infty$ denotes the limit in which the window Ω grows infinitely large in a self-similar fashion (that is, preserving its shape and orientation). The statement in equation (2.2.1) automatically implies that the 2D regular lattice in Figure 2.2b is hyperuniform, and in fact, it is *ordered hyperuniform*. Naturally, the system shown in Figure 2.2c is an example of *disordered hyperuniformity*.

In order to observe the suppression of large scale density fluctuations, the structure factor must satisfy [20]

$$\lim_{|\mathbf{k}|\to 0} S(\mathbf{k}) = 0\,. \tag{2.2.2}$$

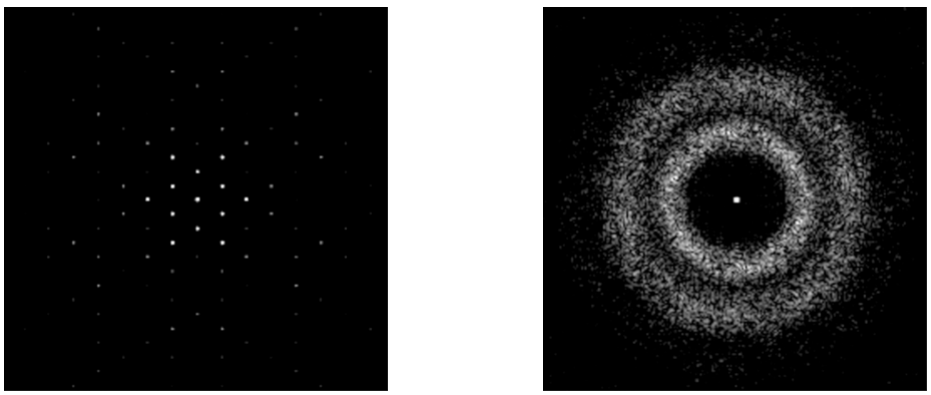

(a) (b)

Figure 2.3: Scattering patterns for two distinctly different hyperuniform systems: (a) a six-fold symmetric crystal and (b) a disordered "stealthy" hyperuniform system. Observe that the stealthy hyperuniform system has no scattering in a circular region around the origin. [21]

As we previously stated, the structure factor is intimately related to the scattering pattern of a material. Figure 2.3a presents a scattering pattern for a six-fold symmetric crystal, showing peaks for certain wavevectors associated with the crystalline structure. Figure 2.3b shows the scattering pattern for a "stealthy" disordered hyperuniform. Stealthy hyperuniformity corresponds to systems in which density fluctuations are suppressed for a range of wavevectors around the origin, i.e.,

$$S(\mathbf{k}) = 0, \qquad 0 < |\mathbf{k}| < K\,, \tag{2.2.3}$$

where K is some positive number. As we observe in figure 2.3b, there is a circular region close to the origin where scattering intensity is exactly zero (discarding forward scattering), a highly exotic situation for an amorphous state of matter.

Now, we will show that the conditions for hyperuniformity expressed in equations (2.2.1) and (2.2.2) are in fact, equivalent. We turn back to equation (2.1.85), and take the infinite window-size limit previously defined, $\mathbf{R} \to \infty$ (that preserves orientation and shape of the window). In this limit, given that the $\Lambda(\mathbf{k}, \mathbf{R}) \to 1$, the Fourier transform $\hat{\Lambda}(\mathbf{k}, \mathbf{R})$ tends to $(2\pi)^n \delta(\mathbf{k})$, with $\delta(\mathbf{k})$, the n-dimensional Dirac delta. Therefore, we can write

$$\lim_{\mathbf{R}\to\infty} \sigma_N^2(\mathbf{R}) = \langle N(\mathbf{R})\rangle \, \frac{1}{(2\pi)^n} \int S(\mathbf{k})(2\pi)^n \delta(\mathbf{k})\, \mathrm{d}\mathbf{k} \tag{2.2.4}$$

$$= \langle N(\mathbf{R})\rangle \, S(\mathbf{k} = \mathbf{0})\,. \tag{2.2.5}$$

Dividing by $\langle N(\mathbf{R})\rangle = \rho_0 V_1(\mathbf{R})$, we obtain

$$\lim_{\mathbf{R}\to\infty} \frac{\sigma_N^2(\mathbf{R})}{\langle N(\mathbf{R})\rangle} = \lim_{|\mathbf{k}|\to 0} S(\mathbf{k})\,. \tag{2.2.6}$$

Hence, the suppression of density fluctuations for small wavenumbers on the structure factor,

$$\lim_{|\mathbf{k}|\to 0} S(\mathbf{k}) = 0\,, \tag{2.2.7}$$

is equivalent to the particle number variance obeying

$$\lim_{\mathbf{R}\to\infty} \frac{\sigma_N^2(\mathbf{R})}{V_1(\mathbf{R})} = 0\,, \tag{2.2.8}$$

that is, particle number variance as a function of window size grows slower than the window volume, in the infinitely large window limit.

2.2.2 Asymptotic scalings and hyperuniformity classes

So far, we are aware of the conditions necessary for hyperuniformity, in particular, that the particle number variance must grow slower than the volume of the observation window. But we do not know how exactly should it behave in the large window size limit. In this section, we will derive the expected scaling laws for σ_N^2 in that limit.

Subsequent results will be given for the case of a n-dimensional spherical (hyperspherical) window of radius R centered at position $\mathbf{x}_0$. Thus, the window indicator function defined in equation (2.1.35) is replaced by the Heaviside step function

$$\Theta(R - |\mathbf{x} - \mathbf{x}_0|) = \begin{cases} 0\,, & |\mathbf{x} - \mathbf{x}_0| > R\,, \\ 1\,, & |\mathbf{x} - \mathbf{x}_0| \leq R \end{cases} \tag{2.2.9}$$

and the window volume becomes

$$V_1(R) = \frac{\pi^{n/2}}{\mathbf{\Gamma}(1 + n/2)} R^n\,, \tag{2.2.10}$$

which is, as expected, the volume of a hypersphere of dimension n and radius R ($\mathbf{\Gamma}(\cdot)$ is the Gamma function).

Let us assume that the structure factor goes to zero in the limit $|\mathbf{k}| \to 0$ with the power-law form

$$S(\mathbf{k}) \sim |\mathbf{k}|^\alpha\,, \tag{2.2.11}$$

where $\alpha > 0$. Note that α cannot be negative for a hyperuniform system, since that would mean that density fluctuations diverge at large scales. Neither can α be zero, otherwise density fluctuations would be constant, and therefore not completetely suppressed in the infinite-wavelength limit. Thus, we wish to obtain the exponent β such that

$$\sigma_N^2(R) \sim R^\beta \tag{2.2.12}$$

in the limit $R \to \infty$, and find the relation between α and β.

Through a series representation of the scaled intersection volume, $\Lambda(r; R)$, it is possible to derive the following asymptotic formula for the particle number variance in the limit $R \to \infty$ [22]:

$$\sigma_N^2(R) = \langle N(R) \rangle \left[A_N(R) + \frac{B_N(R)}{R} + o\big\{(R)^{-1}\big\} \right] \tag{2.2.13}$$

$$= A_N(R) R^n + B_N(R) R^{n-1} + o\big\{(R)^{n-1}\big\}\,, \tag{2.2.14}$$

where $o\{x\}$ denotes all terms of order less than x, and $A_N(R)$ and $B_N(R)$ are n-dependent asymptotic coefficients that multiply terms proportional to the window volume (R^n) and surface area (R^{n-1}), respectively. These *volume* and *surface-area* coefficients are explicitly given by

$$A_N = 1 + \rho_0 \int_{|\mathbf{r}|<2R} h(r)\, \mathrm{d}\mathbf{r}\,, \tag{2.2.15}$$

$$B_N = -\frac{\rho_0 \mathbf{\Gamma}(1 + n/2)}{\mathbf{\Gamma}((n+1)/2)\mathbf{\Gamma}(1/2)} \int_{|\mathbf{r}|<2R} h(\mathbf{r}) |\mathbf{r}|\, \mathrm{d}\mathbf{r}\,. \tag{2.2.16}$$

Note that the restriction on the domain of integration comes from the support of the scaled intersection volume, $\Lambda(r; R)$, and hence results in A_N and B_N generally depending on R.

In the limit $R \to \infty$, the volume coefficient A_N is equal to the structure factor $S(\mathbf{k})$ in the zero-wavenumber limit, *i.e.*,

$$\overline{A}_N \equiv \lim_{R\to\infty} A_N = \lim_{|\mathbf{k}|\to 0} S(\mathbf{k})\,. \tag{2.2.17}$$

We call $\overline{A}_N$, the *global* volume coefficient. Accordingly, a hyperuniform system is one in which the global volume coefficient vanishes, that is,

$$\overline{A}_N = \lim_{|\mathbf{k}|\to 0} S(\mathbf{k}) = 0\,. \tag{2.2.18}$$

Disordered point configurations associated with equilibrium molecular systems with a variety of interaction potentials (e.g., hard-sphere, square-well, and Lennard-Jones) yield positive values of the coefficient $\overline{A}_N$ in gaseous, liquid, and many solid states. Indeed, because of the fluctuation-compressibility theorem [19], any equilibrium system with a strictly positive compressibility will have a strictly positive volume coefficient, and therefore be nonhyperuniform.

Given that the structure factor and the total correlation function are related by the Fourier transform, if one follows a power law, so does the other, with the exponents related by the dimension of the space. Indeed, given that we assumed $S(\mathbf{k}) \sim |\mathbf{k}|^{\alpha}$, then

$$h(\mathbf{r}) \sim \frac{1}{r^{n+\alpha}}\,, \tag{2.2.19}$$

for $r \equiv |\mathbf{r}| \to \infty$. We will use this expression to calculate the asymptotic value of the surface-area coefficient, $B_N(R)$. Taking the lower limit of the integral to be some (large-value) r_0 and the upper limit to be R, equation (2.2.16) yields

$$B_N(R) \sim \int_{r_0}^{R} \frac{1}{r^{n+\alpha}} r\,\mathrm{d}\mathbf{r}\,, \tag{2.2.20}$$

and using that $\mathrm{d}\mathbf{r} \sim r^{n-1}\,\mathrm{d}r$ (in euclidean $\mathbb{R}^n$ space), we obtain

$$B_N(R) \sim \int_{r_0}^{R} \frac{1}{r^{n+\alpha}} |r|^n\,\mathrm{d}r \tag{2.2.21}$$

$$\sim \int_{r_0}^{R} \frac{\mathrm{d}r}{r^{\alpha}}\,. \tag{2.2.22}$$

Now, there are three cases for α, which will allow us to define distinct hyperniformity classes:

- If $\alpha > 1$, given that $R \to \infty$, the last integral converges to a constant which we will denote $\overline{B}_N$, the *global* surface-area coefficient. Therefore, equation (2.2.14) yields

  $$\sigma_N^2 \sim \overline{B}_N R^{n-1}\,, \tag{2.2.23}$$

  and then $\beta = n - 1$. Any system in which the surface-area coefficient converges to a constant is a class I hyperuniform system. This includes not only systems with a total correlation function that scales as in equation (2.2.19), but also any other with $h(r)$ decaying sufficiently fast. Examples of class I hyperuniformity are perfect crystals and a large group of perfect quasicrystals, all of which are characterized by Bragg peaks in reciprocal space, and additionally, stealthy disordered hyperuniform patterns and some disordered point configurations in which the total correlation function decays exponentially fast or faster, or at least faster than $1/|\mathbf{r}|^{n+1}$, [2].

- If $\alpha = 1$, then the integral in equation (2.2.22) yields $B_N(R) \sim \log R$, and therefore

$$\sigma_N^2 \sim R^{n-1} \log R \,, \tag{2.2.24}$$

which we refer to as class II hyperuniformity. Examples include some quasicrystals [23], density fluctuations in early Universe mentioned before [3], maximally random jammed packings [8, 10], zeros of the Riemann zeta function and eigenvalues of random matrices [24], superfluid helium [25] and perfect glasses [26].

- Finally, if $0 < \alpha < 1$, from equation (2.2.22) we obtain $B_N(R) \sim R^{1-\alpha}$. Thus,

$$\begin{aligned} \sigma_N^2 \sim & B_N(R) R^{n-1} && (2.2.25)\\ \sim & R^{1-\alpha} R^{n-1} && (2.2.26)\\ = & R^{n-\alpha} \,, && (2.2.27) \end{aligned}$$

and consequently, $\beta = n - \alpha$, which defines class III hyperuniformity. Examples within this class include critical absorbing states [27], perfect glasses [26], and perturbed lattices [28].

Summarizing, if $S(\mathbf{k}) \sim |\mathbf{k}|^\alpha$, then the particle number variance has the large-scale behavior:

$$\sigma_N^2 = \begin{cases} R^{n-1} \,, & \alpha > 1 \qquad \text{(Class I)} \\ R^{n-1} \log R \,, & \alpha = 1 \qquad \text{(Class II)} \\ R^{n-\alpha} \,, & 0 < \alpha < 1 \qquad \text{(Class III)} \end{cases} \tag{2.2.28}$$

2.2.3 Other characterizations

In heterogeneous media, the particle number variance is not well suited to detect the suppresion of density fluctuations in real space. An alternative formulation of hyperuniformity involves the variance of the local volume fraction

$$\sigma_{\tau_i}^2(R) = \left\langle \tau_i(R)^2 \right\rangle - \phi_i^2 \,, \tag{2.2.29}$$

where τ_i is the local volume fraction of phase i inside a n-dimensional spherical window of radius R, and ϕ_i is the (usual) global volume fraction of phase i. The local volume fraction is defined as

$$\tau_i(\mathbf{x}_0; R) = \frac{1}{V_1(R)} \int F_i(\mathbf{x}) \upsilon(\mathbf{x} - \mathbf{x}_0; R) \, \mathrm{d}\mathbf{x} \,, \tag{2.2.30}$$

where

$$F_i(\mathbf{x}) = \begin{cases} 1 \,, & \mathbf{x} \text{ in phase } i \,, \\ 0 \,, & \mathbf{x} \text{ not in phase } i \end{cases} \tag{2.2.31}$$

is the phase indicator function. Non-hyperuniform disordered media, such as typical liquids or glases, have the scaling $\sigma_\tau^2 \sim R^{-n}$. By contrast, a hyperuniform system will have volume-fraction fluctuations decreasing faster than R^{-n}. This description has been proven succesful in identifying hyperuniformity in colloids [10] or polymers [29], since it takes into account the dissimilar volume fraction of multi-phase media or the size of particles in polydisperse systems.

There are other situations where neither σ_N^2 nor $S(k)$ have been found useful in characterizing the suppression of density fluctuations at large scales. Quasicrystals, which lack periodicity but have long-range order, are expected to present hyperuniformity. However, it has been shown that it is impossible to observe it through the structure factor (which is discontinuous), and instead, a cumulative or integrated intensity function must be defined, which displays the expected scaling [23]. In jammed packings of polydisperse spheres, the structure factor does not decay to zero for small wavenumbers, but rather the compressibility [9].

Chapter 3

Diffusion in granular systems

Phenomenologically, diffusion is the movement of a substance from a region of higher concentration to a region of lower concentration, withour involving bulk motion (i.e., without advection). The term commonly refers to the intermixture of the components of two or more substances, but henceforth we will use diffusion refering to *self-diffusion*: the spreading of the components of a single substance.

Driven granular media has long been recognized to have properties similar to those of ordinary fluids. In the same fashion as concentration gradients in a liquid induce diffusion of the molecules, the constituents of a fluidized granular system could be expected to diffuse from regions of higher to lower agitation. As a matter of fact, there has been extensive work on this matter, with expertimental studies of diffusion in granular shear flows [30, 31] and fluidized beds [32], and the development of theory and simulations of diffusion in granular fluids [33, 34, 35, 36], to name a few examples.

In Section §3.1 we review Fick's laws of diffusion, namely the definition of the diffusion coefficient, and the derivation of the diffusion equation. Then, in Section §3.2 we define the mean square displacement of particles and derive its relation to the diffusion coeffcient. Finally, in Section §3.3, we make a brief account on the concept of granular temperature.

3.1 The laws of diffusion

The laws governing the transport of mass through diffusive means were first reported by Adolf Fick in 1855 [37]. Based on the previous work of Thomas Graham on diffusion of gases (1833), Fick's experiments consisted in measuring the concentrations and fluxes of salt, diffusing between a reservoir through a water tube, and into fresh water. These experiments allowed Fick to derive his first law, concerning the relation between the flux of a substance and the concentration gradient, as well as his second law, commonly known as the diffusion equation.

3.1.1 Fick's first law

We will reproduce a simple derivation of Fick's first law from random walks, as done by Howard Berg [38]. Consider a collection of particles moving randomly in 1D, within a length scale Δx and time Δt. Let $N(x,t)$ be the number of particles at position x and time t. Then, at a time t, half of the particles at x would have crossed to the left of the cross section A (perpendicular to the x axis), while half of the particles at $x+\Delta x$ would have crossed to the right of the cross section A (See Figure 3.1). Thus, the net number of particles crossing to the right will be $-\frac{1}{2}(N(x+\Delta x,t)-N(x,t))$. To obtain the net flux, we divide by the cross section area A, and the time interval Δt

$$J_x(x,t) = -\frac{1}{2}\left(\frac{N(x+\Delta x,t)-N(x,t)}{A\Delta t}\right). \tag{3.1.1}$$

Now, we multiply by $(\Delta x)^2/(\Delta x)^2$ and rearrange, obtaining

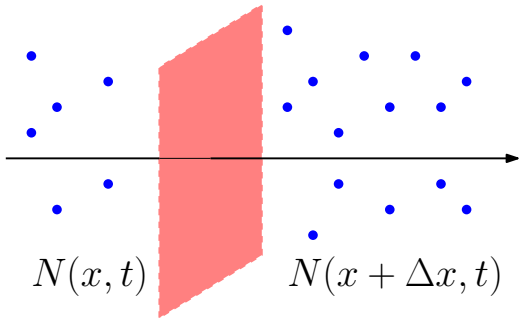

Figure 3.1: Diagram for derivation of the diffusion equation. $N(x,t)$ is the number of particles at position x and time t.

$$J_x(x,t) = -D\frac{1}{\Delta x}\left(\frac{N(x+\Delta x,t)}{A\Delta x} - \frac{N(x,t)}{A\Delta x}\right), \tag{3.1.2}$$

where $D \equiv \frac{(\Delta x)^2}{2\Delta t}$is the diffusion coefficient. Note that we can define $\rho(x,t) \equiv \frac{N(x,t)}{A\Delta x}$ as the number density (or concentration), i.e. the number of particles per unit volume at position x and time t. Therefore, we rewrite the last equation as

$$J_x(x,t) = -D\left(\frac{\rho(x+\Delta x,t)-\rho(x,t)}{\Delta x}\right). \tag{3.1.3}$$

Taking the limit $\Delta x \to 0$, yields

$$J_x = -D\frac{\partial \rho}{\partial x}. \tag{3.1.4}$$

This equation, known as Fick's first law, states that the net flux is proportional to the negative of the slope of the concentration. If the particles are uniformly distributed, there is no gradient, and therefore the flux is zero. If there is a concentration gradient, particles diffuse from higher concentration regions to lower concentration regions. Extending this equation to the 3D case is straightforward

$$\mathbf{J} = -D\boldsymbol{\nabla}\rho, \tag{3.1.5}$$

where we have used $J_y = -D\frac{\partial \rho}{\partial y}$ and $J_z = -D\frac{\partial \rho}{\partial z}$. Note that here we have assumed the system is isotropic. In anisotropic media, D depends on the direction, so it becomes a symmetric tensor $D = D_{ij}$, changing Fick's first law to

$$J_i = -D_{ij}\frac{\partial \rho}{\partial x_j}\,, \tag{3.1.6}$$

where Einstein's notation is applied.

3.1.2 Diffusion equation

In order to derive Fick's second law, we make use of the continuity equation, which reflects the conservation of mass in the system. This equation is derived by adding up the rate at which mass is flowing in and out of a control volume $\mathrm{d}V$, and setting the net flow equal to the rate of change of mass within it, $\frac{\partial \rho}{\partial t}\,\mathrm{d}V$ (see figure 3.2).

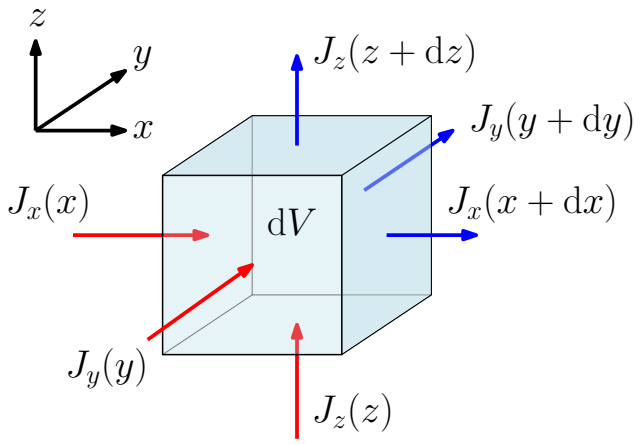

Figure 3.2: Scheme for the derivation of the continuity equation. Red arrows are incoming flux, blue arrows are outgoing flux. As an example, the net mass change in the x direction is equal to $J_x(x) - J_x(x+\mathrm{d}x)$.

Let $\mathbf{J}$ be the mass flux. Equating the mass flow rates into and out of the differential control volume, we obtain

$$\begin{aligned}
(J_x(x) - J_x(x+\mathrm{d}x))\,\mathrm{d}y\,\mathrm{d}z + (J_y(y) - J_y(y+\mathrm{d}y))\,\mathrm{d}z\,\mathrm{d}x \\
+(J_z(z) - J_z(z+\mathrm{d}z))\,\mathrm{d}x\,\mathrm{d}y = \frac{\partial \rho}{\partial t}\,\mathrm{d}V
\end{aligned} \tag{3.1.7}$$

$$\begin{aligned}
-\frac{(J_x(x+\mathrm{d}x) - J_x(x))}{\mathrm{d}x}\,\mathrm{d}y\,\mathrm{d}z\,\mathrm{d}x - \frac{(J_y(y+\mathrm{d}y) - J_y(y))}{\mathrm{d}y}\,\mathrm{d}z\,\mathrm{d}x\,\mathrm{d}y \\
-\frac{(J_z(z+\mathrm{d}z - J_z(z)))}{\mathrm{d}z}\,\mathrm{d}x\,\mathrm{d}y\,\mathrm{d}z = \frac{\partial \rho}{\partial t}\,\mathrm{d}V
\end{aligned} \tag{3.1.8}$$

$$\begin{aligned}
-\left(\frac{(J_x(x+\mathrm{d}x) - J_x(x))}{\mathrm{d}x} + \frac{(J_y(y+\mathrm{d}y) - J_y(y))}{\mathrm{d}y}\right. \\
\left. +\frac{(J_z(z+\mathrm{d}z - J_z(z)))}{\mathrm{d}z}\right)\mathrm{d}x\,\mathrm{d}y\,\mathrm{d}z = \frac{\partial \rho}{\partial t}\,\mathrm{d}V\,.
\end{aligned} \tag{3.1.9}$$

Note that the fractions in the last expression are just the partial derivatives of the components of $\mathbf{J}$. Dividing through by $\mathrm{d}V = \mathrm{d}x\,\mathrm{d}y\,\mathrm{d}z$ yields

$$-\left(\frac{\partial J_x}{\partial x} + \frac{\partial J_y}{\partial y} + \frac{\partial J_z}{\partial z}\right) = \frac{\partial \rho}{\partial t}\,. \tag{3.1.10}$$

Writing in vector notation, we obtain the continuity equation

$$\frac{\partial \rho}{\partial t} = -\nabla \cdot \mathbf{J}\,. \tag{3.1.11}$$

It should be noted that the derivation above works as long as there are no sources or sinks for particles to be created or destroyed. Now, replacing equation (3.1.5)

$$\frac{\partial \rho}{\partial t} = -\nabla \cdot (-D\boldsymbol{\nabla}\rho)\,, \tag{3.1.12}$$

we obtain the diffusion equation

$$\frac{\partial \rho}{\partial t} = D\nabla^2\rho\,. \tag{3.1.13}$$

In the last step, we have assumed that D is independent of the position in space. If $D = D(x, y, z)$, Fick's first law is unaffected, but the diffusion equation must be changed to

$$\frac{\partial \rho}{\partial t} = \nabla \cdot (D\boldsymbol{\nabla}\rho)\,. \tag{3.1.14}$$

3.2 Mean square displacement and diffusion

The mean square displacement (MSD) represents the deviation of the position of a particle with respect to a reference position, over time. A measure of the MSD of a system allows us to determine what kind of tranport governs the system on a given time-scale, be it ballistic, diffusive, advective, etc.

In a diffusive system, the diffusion coefficient is closely related to the MSD of particles as a function of time. We assume the particles are at position $\mathbf{r} = 0$ when $t = 0$, so the MSD at time t can be expressed as

$$\left\langle (\mathbf{r}(t))^2 \right\rangle = \frac{1}{N}\int (\mathbf{r}(t))^2 \rho(\mathbf{r}, t)\,\mathrm{d}\mathbf{r}\ , \tag{3.2.1}$$

where $N = \int \rho(\mathbf{r}, t)\,\mathrm{d}\mathbf{r}$ is the total number of particles, which we assume constant. Now, multiplying equation (3.1.13) by r^2/N and integrating over $\mathrm{d}\mathbf{r}$, yields

$$\frac{\partial}{\partial t}\frac{1}{N}\int \mathbf{r}^2\rho\,\mathrm{d}\mathbf{r} = \frac{D}{N}\int r^2\nabla^2\rho\,\mathrm{d}\mathbf{r}\ . \tag{3.2.2}$$

Noting that the LHS is equal to the total time derivative of the MSD, we rewrite the last equation

$$\frac{\mathrm{d}}{\mathrm{d}t}\left\langle (\mathbf{r}(t))^2 \right\rangle = \frac{D}{N}\int r^2\nabla^2\rho\,\mathrm{d}\mathbf{r}\ . \tag{3.2.3}$$

For the RHS, we consider a surface S confining the system, and then apply Green's theorem to ρ and r^2

$$\int \left(r^2\nabla^2\rho - \rho\nabla^2 r^2\right) \mathrm{d}\mathbf{r} = \int_S \left(r^2\frac{\partial\rho}{\partial\mathbf{e}} - \rho\frac{\partial r^2}{\partial\mathbf{e}}\right) \cdot \mathrm{d}S\,\mathbf{e}\,, \tag{3.2.4}$$

where $\mathbf{e}$ is the unit vector normal to the surface S. Now, if we put the surface S at infinity, where the particle density ρ vanishes, the surface integral in the last equation becomes zero, yielding

$$\int r^2\nabla^2\rho\,\mathrm{d}\mathbf{r} = \int \rho\nabla^2 r^2\,\mathrm{d}\mathbf{r}\ . \tag{3.2.5}$$

Using the last equality and the fact that $\nabla^2 r^2 = 2n$ (with $n = 1, 2, 3$ the dimensionality of the system), equation (3.2.3) reads

$$\frac{\mathrm{d}}{\mathrm{d}t}\left\langle(\mathbf{r}(t))^2\right\rangle = \frac{2nD}{N}\int \rho\,\mathrm{d}\mathbf{r}\ . \tag{3.2.6}$$

But the integral in the RHS is just the definition of N, hence

$$\frac{\mathrm{d}}{\mathrm{d}t}\left\langle(\mathbf{r}(t))^2\right\rangle = 2nD\,. \tag{3.2.7}$$

Integrating in time, we get the relation between the MSD and the diffusion coefficient, as a function of time

$$\left\langle(\mathbf{r}(t))^2\right\rangle = 2nDt\,. \tag{3.2.8}$$

3.3 Granular temperature

Temperature, in the usual sense, does not play a relevant role in the dynamics of granular systems. This is due to the large scale of grains in comparison to the scales of molecules and their kinetic energy. Despite this fact, it is possible to define a *granular temperature* [39, 40, 41]

$$T = \left\langle\delta\mathbf{v}^2\right\rangle\ , \tag{3.3.1}$$

where $\delta\mathbf{v} = \mathbf{v} - \mathbf{u}$ is the fluctuating velocity of a grain, $\mathbf{v}$ is its instantaneous velocity, and $\mathbf{u}$ is the average velocity of the system. Thus, T represents twice the energy per unit mass contained in the random motion of the particles. If there is no net flow of the grains in a particular direction (no advection), $\mathbf{u} \sim \mathbf{0}$ and we can rewrite

$$T = \left\langle\mathbf{v}^2\right\rangle\ . \tag{3.3.2}$$

The concept of granular temperature allows to exploit the analogy between the random motion of fluidized grains and the thermal motion of molecules. But despite having provided useful results since it was first introduced in the late 1970s, it has been a controversial matter to this day [42]. One of the reasons for this polemic is that T_G is not a thermodynamic property, but rather a steady state constant determined by grains' complex dynamics. Since particle collisions in granular matter are inelastic, granular temperature can only be a dynamic constant as long as power is supplied to the system to balance energy dissipation. Otherwise,

the system will quickly come to rest in an *homogeneous cooling state*, characterized by Haff's law [43]. Furthermore, in kinetic theory of gasses the imposition of equipartition of energy on the Maxwell distribution results in the usual definition of thermal temperature. But equipartition of energy is not valid for non-equilibrium systems: rotational and translational temperatures of granular gases with tangential restitution do not equal each other [44], and neither do the temperatures of the constituents of a granular mixture [45, 46]. Another issue with the notion of a granular temperature is the lack of strong scale separation that characterizes molecular fluids. Even for large temperature gradients, over many interparticle distances or mean free paths the temperature can be considered to be nearly constant, which is why a macroscopic thermometer provides a meaningul measure. However, there is no known granular thermometer or a direct way to measure T_G. The granular temperature of a system must be found through direct measurement or calculation of the grains velocities. Despite the arguments described so far, the use of granular temperature in several granular systems has proven to be highly succesful and can lead to useful analysis of granular gasses and fluids.

By means of kinetic theory, a relation can be derived between the diffusion coefficient and the temperature. For hard sphere liquids [19], the diffusion coefficient is proportional to the square root of the ordinary temperature. Granular gases in the homogeneous cooling state [43, 33], granular shear flows [30, 31] and granular fluidized beds [32] have shown the same behavior with respect to the granular temperature

$$D \propto T^{1/2} . \tag{3.3.3}$$

Chapter 4

Experimental methods

In this chapter we describe the experimental setup, main procedures and computational tools used in our experiments. In Section §4.1, we describe the existing setup used in preceeding works, and the improvements made during the development of this thesis. In Section §4.2, we present the methods used to detect and track particles.

4.1 Experimental setup

The experimental setup has been previously reported [11, 12, 13]. It consists of a collection of grains confined in a quasi-2D box, which is vibrated sinusoidally in the vertical direction. Images of the system are taken with a high-speed camera and then analyzed in order to detect the positions of the grains and follow their trajectories. Henceforth, we describe in detail the existing experimental setup and the upgrades done to improve it.

4.1.1 Existing setup

A schematic of the experimental setup is shown in Figure 4.1. The granular system is composed of $N = 11704$ stainless steel spherical particles of diameter $a = 1\,\text{mm}$, confined by a quasi-2D box with lateral dimensions $L_x = L_y \equiv L = 100a$. The height of the box is $L_z = (1.94 \pm 0.02)a$, allowing particles to partially mount without jumping over each other. The lateral walls are provided by a square steel frame with a thin mylar sheet frame on top, both resting between two 10 mm thick glass plates, which form the top and bottom walls of the box. These plates are internally coated with an ITO (Indium Tin Oxide) nano-layer, with the purpose of dissipating electrostatic charges and thus avoiding any electric interactions between the grains. The quasi-2D box is contained in a steel cell, which supports an array of LEDs below the bottom wall of the box, with a white acrylic diffusor in between. This allows us to illuminate the particles from below, which has the advantage of giving a better contrast for detection of dense clusters. The cell, placed over an optical table, is forced sinusoidally with an electro-mechanical shaker located underneath, with displacement $z(t) = A\sin(\omega t)$ and frequency $f = \omega/2\pi = 80\,\text{Hz}$. For all the measurements done in this thesis the number of particles N, the height of the cell L_z and the driving frequency f are kept fixed. A 30 cm long threaded rod connects the cell to the shaker, going through a cylindrical air bearing system mounted in a hole at the center of the table. An accelerometer, fixed to the base of the cell, allows us to measure of the forcing amplitude imposed on the system.

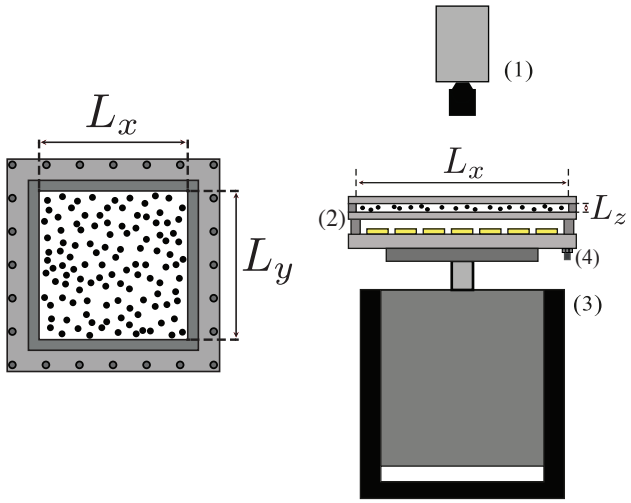

Figure 4.1: Schematic of the experimental setup. (left) Top view of the quasi-2D cell, with $L_x = L_y = 100a$. (right) Side view of the setup. The vertical height in the cell is $L_z = (1.94 \pm 0.02)a$. The cell is illuminated from below with a 2D array of LEDs, where light is diffused with a white acrylic sheet placed between the array and the cell. (1) camera, (2) quasi-2D cell, (3) electromechanical shaker, (4) accelerometer.

The motion of the electromechanical shaker (Vibration Test Systems VG 80A-6) is induced by a sinusoidal signal produced by a waveform generator (Rigol DG 2041A). The signal is sent to a sound amplifier (Crown XTi 2000) in order to supply the necessary power for the shaker. The piezoelectric accelerometer (B&K 4393), attached to the bottom of the cell, measures the acceleration of the system. The signal provided by this device is conditioned by a charge amplifier (B&K 2635), and then sent to a lock-in amplifier (Stanford Research Systems SR830 DSP). Then, by GPIB (General Purpose Interface Bus), the lock-in amplifier is connected to a computer where the raw voltage data is converted to acceleration and analized with a LabView virtual instrument. This program computes the mean value and standard deviation of $\Gamma \equiv A\omega^2/g$, the adimensional acceleration, which serves as the control parameter. An oscilloscope (Tektronix TDS 2012) is used to monitor both the voltage signal sent to the shaker and the response of the system measured by the accelerometer.

We acquire top view images with a high-speed camera (Phantom v641) at a resolution of $1600 \times 1600\,\mathrm{pix}^2$ using two sample rates, depending on the quantities we wish to calculate. For quantities we need to track over time, we record at 500 fps, while for static quantities, we measure at 10 fps to avoid correlation between consecutive images. A sample image acquired with the camera is displayed in figure 4.2. The typical diameter of a particle in an image is $d \sim 16\,\mathrm{pix}$, and our acquisitions are typically 3000 images long. This implies recording times of 6 s for videos at 500 fps and 5 min for videos at 10 fps.

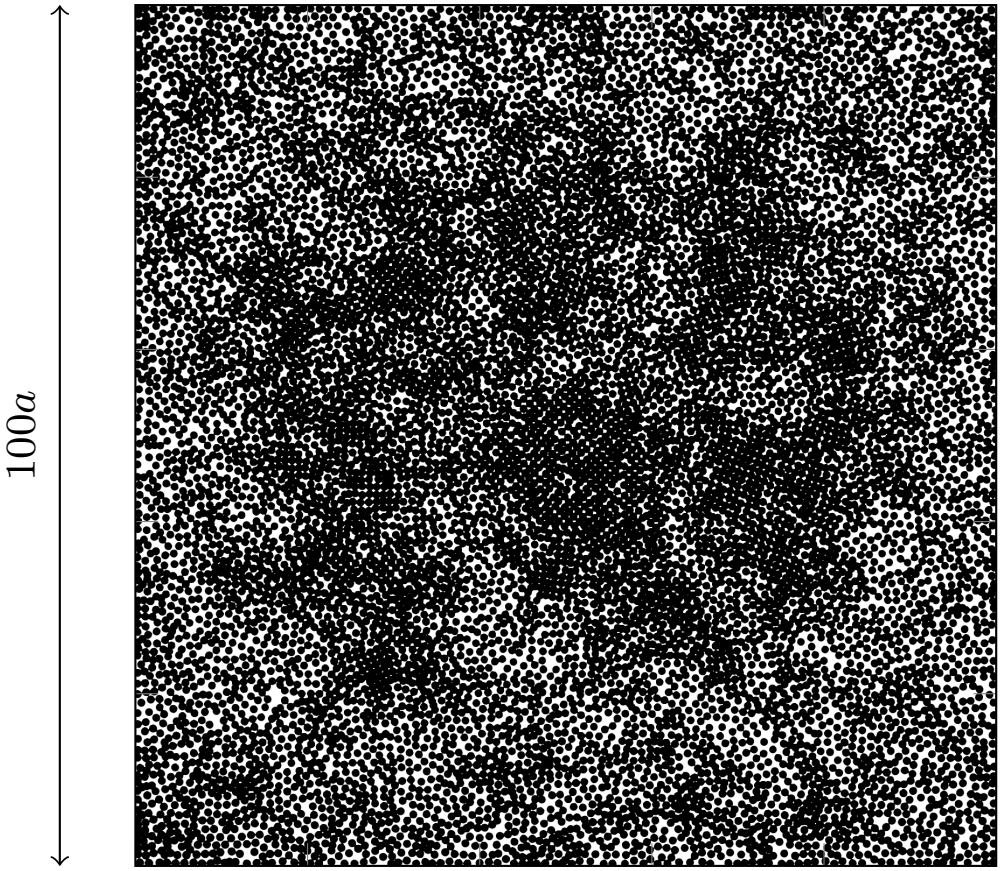

Figure 4.2: Raw image of the system, captured at a resolution of $1600 \times 1600\,\mathrm{pix}^2$. Particles are seen as black circles in a white background, due to illumination being placed behind the cell. The diameter of a particle is $\sim$ 16pix.

4.1.2 Upgrade on the camera support

In previous works, the camera was supported by a tripod placed over the table. This caused some minor issues at the moment of focusing the camera and framing the cell, since any disturbance would displace the tripod and misalign the frame. In order to overcome this difficulty, we designed a support structure for the camera that provides stability and precision to frame the picture. Additionally, this upgrade allowed us to considerably reduce the time spent on setting up the experiment for measurements.

The structure designed to support the camera is shown in Figure 4.3. A rectangular frame built with T-slotted aluminium profiles is attached to two vertically placed posts of the same material. The T-slots, along with matching nuts, allow to change the height of the rectangular frame, depending on the desired focus of the camera. An aluminium alloy platform rests on top of the rectangular frame, and can be slid for coarse horizontal adjustment of the camera.

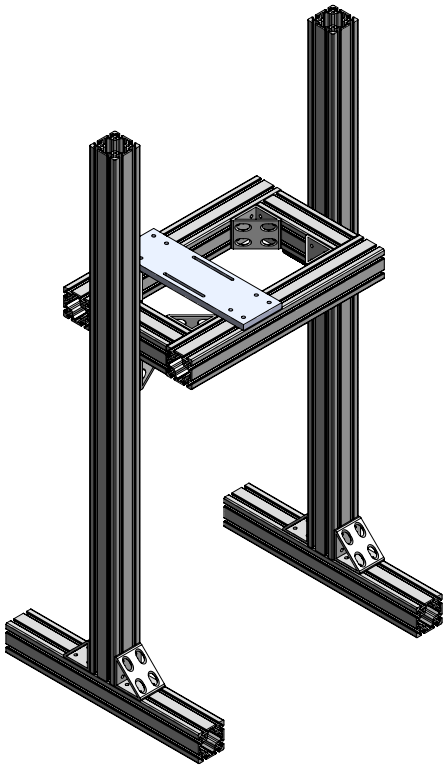

Figure 4.3: Support structure for the camera, with overall height of 1.5 m. Two vertical aluminium T-slotted profiles support a rectangular frame of the same material, with adjustable height. An aluminium alloy plate rests on top of the rectangular frame. The whole structure is located on top of an optical table that supports the cell.

Thorlabs XYZ manual stages are secured to the platform on top of the structure in order to hold the camera, allowing 3D lineal displacement with milimetric precision. An additional Thorlabs rotational stage is included in order to allow the rotation of the camera (See Figure 4.4).

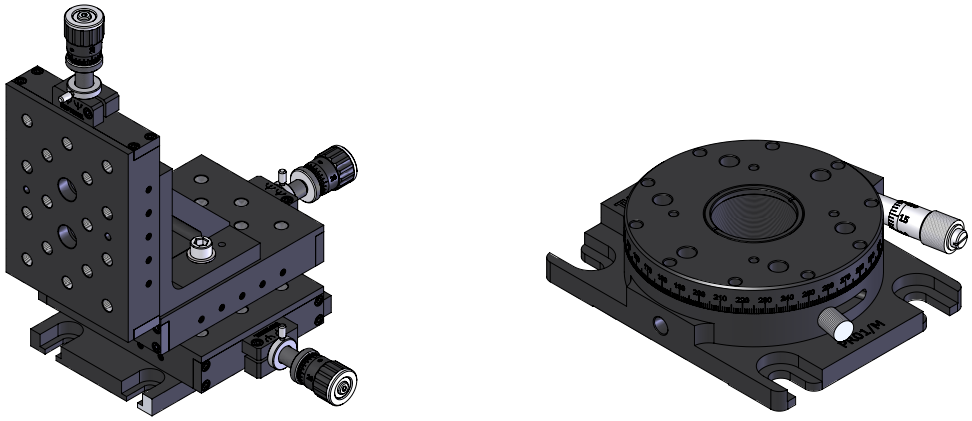

(a) (b)

Figure 4.4: Thorlabs manual stages for (a) linear XYZ millimetric displacement, and (b) rotation. The rotational stage is placed between the XY stages and the Z stage [47, 48].

In order to couple the camera to these Thorlabs stages, another two alluminium alloy pieces were designed and built (See Figure 4.5). One of the pieces is attached to the camera, and then slid into the other piece, which is fixed to the vertical Thorlab stage.

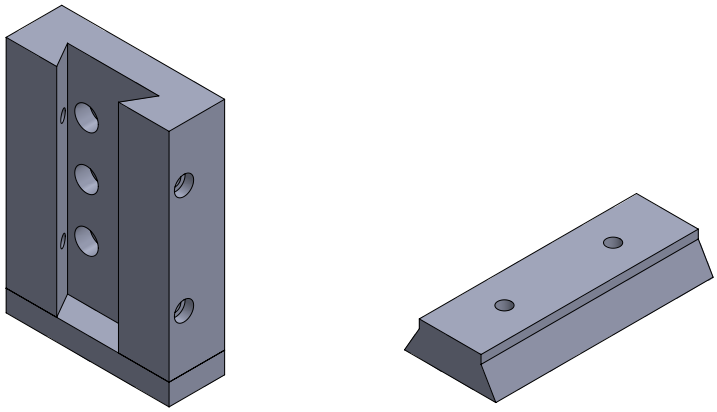

(a) (b)

Figure 4.5: Aluminium alloy pieces fabricated to couple the camera to Thorlabs stages. Piece (a) is fixed to the Thorlabs Z stage. Piece (b) is fixed to the camera and then slid in the slot of piece (a). Lateral through holes in piece (a) allow to fix the two pieces together with screws.

4.2 Image analysis

In this section, we outline the algorithms used in order to detect particles and their trajectories from the images previously acquired. The algorithm for detection is based on a least-square fit, and involves the convolution of the image with a function that represents an idealized particle. In order to obtain the trayctories of the particles, we use a combinatorial algorithm that matches the positions of the particles between consecutive images.

4.2.1 Particle detection

We describe the algorithm used for detection, based on a least-square fit (LSQ) and developed by Mark Shattuck [49]. Let us assume that the image to be tracked is of the form

$$I_{exp}(\mathbf{x}) = \sum_{j=1}^{N} I_p^*(\mathbf{x} - \mathbf{x_j}; d, \ldots)\,, \tag{4.2.1}$$

where N is the number of particles, $\mathbf{x_j}$ is the position of particle j and $I_p^*(\mathbf{x}; d, \ldots)$ is a function describing the shape of a particle centered at the origin. This function may depend on the diameter of the particle d or any other properties of the particles or the imaging system. In order to track particles with actual shape, I_p^*, in an image described by equation (4.2.1), an ideal particle function I_p is defined. For spherical particles imaged in backlighting and normalized so that the particles are bright, an ideal particle may be represented by the function

$$I_p(\mathbf{x}; d, w) = \left[1 - \tanh\left(\frac{|\mathbf{x}| - d/2}{w}\right)\right]/2\,, \tag{4.2.2}$$

where d is the particle diameter, and w is a parameter that represents the width of the transition between the black particle and the white background (See Figure 4.6). This parameter depends strongly on the focus of the image; a value of $w \sim 1\,\text{pix}$ indicates a very sharp image, while $w > 1$ is a sign of blurriness.

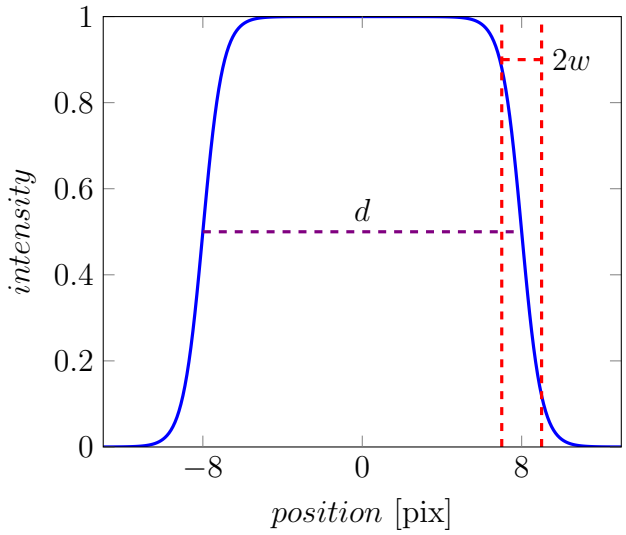

Figure 4.6: Function definition for an ideal particle with diameter d. The parameter w is related to the focus of the image.

The basic idea of LSQ is to compare the actual image to a calculated image based on equation (4.2.1) and find the positions and parameters that minimize the difference. In that way, the LSQ determines the most likely position of a particle (that is, the position $\mathbf{x_0}$ that minimizes the weighted squared difference between the actual image $I(\mathbf{x})$ and the calculated ideal particle image $I_p(\mathbf{x} - \mathbf{x}_0)$. Specifically, the minimum of the weighted squared difference χ^2 is given by

$$\chi^2(\mathbf{x}_0; d, w) \equiv \int W(\mathbf{x} - \mathbf{x}_0)[I(\mathbf{x}) - I_p(\mathbf{x} - \mathbf{x}_0; d, w)]^2 \mathrm{d}\mathbf{x}\,, \tag{4.2.3}$$

where $\mathbf{x}_0$ is a particle center, W is a weight function and the integration domain correponds to the area of the experimental image I. However, it should be noted that the domain of $\mathbf{x}_0$ is larger. In general, if the size of the image is L_x by L_y and the size of I_p is s_x by s_y then the range of integration is $[0, L_x]$ and $[0, L_y]$, but the range of $\mathbf{x}_0$ is $[-s_x, L_x + s_x]$ and $[-s_y, L_y + s_y]$. When $\mathbf{x}_0$ is the position of a particle center, then χ^2 will be minimum. Therefore, minimizing χ^2 over $\mathbf{x}_0$ will produce the particle's position. In fact, if all of the particles are the same then there will be a minimum in χ^2 at the position of each particle. If the image was given by equation (4.2.1) with $I_p^* = I_p$ then χ^2 would be zero for each $\mathbf{x}_0 = \mathbf{x}_j$. The process of finding the particles is equivalent to finding all of the minima of χ^2. Expanding equation (4.2.3) we obtain

$$\chi^2(\mathbf{x}_0; d, w) = \int W(\mathbf{x} - \mathbf{x}_0)\left[I^2(\mathbf{x}) - 2I(\mathbf{x}) \cdot I_p(\mathbf{x} - \mathbf{x}_0; d, w) + I_p^2(\mathbf{x} - \mathbf{x}_0; d, w)\right], \tag{4.2.4}$$

$$\chi^2(\mathbf{x}_0; d, w) = I^2 \otimes W - 2I \otimes (WI_p) + \left\langle WI_p^2 \right\rangle\,, \tag{4.2.5}$$

where

$$f \otimes g = [f \otimes g](\mathbf{x}_0) \equiv \int f(\mathbf{x}) g(\mathbf{x} - \mathbf{x}_0) \mathrm{d}\mathbf{x} \tag{4.2.6}$$

is a modified cross-correlation and $\langle f \rangle = 1 \otimes f$. Observe that $\langle f \rangle$ is a function of $\mathbf{x}_0$, since the domain of integration is over the image only. Assuming that W and I_p are symmetric, we can evaluate equation (4.2.6) using convolutions, which are defined as

$$f * g = [f * g](\mathbf{x}_0) \equiv \int f(\mathbf{x}) g(\mathbf{x}_0 - \mathbf{x}) \mathrm{d}\mathbf{x} \,. \tag{4.2.7}$$

Therefore,

$$f \otimes g = [f(\mathbf{x}) \otimes g(\mathbf{x})](\mathbf{x}_0) = [f(\mathbf{x}) * g(-\mathbf{x})](-\mathbf{x}_0) \,. \tag{4.2.8}$$

Several choices are possible for the weight function. If $W = 1$, then

$$\chi^2(\mathbf{x}_0; d, w) = \int I^2 \mathrm{d}\mathbf{x} - 2I \otimes I_p + \left\langle I_p^2 \right\rangle \,. \tag{4.2.9}$$

In this case, the first term does not depend on $\mathbf{x}_0$ and the last term only depends on $\mathbf{x}_0$ near the borders of the image. Thus, $I \otimes I_p$ will be maximum wherever $\mathbf{x}_0$ is the particle's position. This cross-correlation alone works well for images in which the particles are well separated and have good signal to noise. This is because the weight function is very broad making the fit sensitive to the fact that the ideal particle image has zeros all around it, in contrast with the real image, in which other particles are nearby. Given that information from the images is provided in pixels, the positions obtained will likely be accurate to a pixel. In order to get better resolution, a more compact weight function is needed. Choosing the weight function to be the ideal particle itself, $W = I_p$, then equation (4.2.5) becomes

$$\chi^2(\mathbf{x}_0; d, w) = I^2 \otimes I_p - 2I \otimes I_p^2 + \left\langle I_p^3 \right\rangle \,. \tag{4.2.10}$$

The first term shows that only the area of size I_p around each point $\mathbf{x}_0$ is important. The last term is constant except near the edges of the image. Near the edge, all terms get smaller due to the fact that there is less overlap between the experimental image I and the region of interest I_p. Dividing through by the last term normalizes this effect at the boundary, which we use to redefine χ^2,

$$\chi^2(\mathbf{x}_0; d, w) \equiv \frac{I^2 \otimes I_p - 2I \otimes I_p^2}{\left\langle I_p^3 \right\rangle} + 1 \,. \tag{4.2.11}$$

This normalized χ^2 is still minimized at the positions of the particles and allows us to find particles that have centers outside of the image. As we mentioned before, LSQ gives particle centers to approximately one pixel accuracy. However, using LSQ on the whole image allows significantly higher sub-pixel accuracy. To do this, we will look for a modified fitting function

$$\chi^2(\mathbf{x}_j; d, w) = \int [I(\mathbf{x}) - I_c(\mathbf{x} - \mathbf{x}_j)]^2 \mathrm{d}\mathbf{x} \,, \tag{4.2.12}$$

where $I(\mathbf{x})$ is the image to be tracked, and

$$I_c(\mathbf{x} - \mathbf{x}_j) = \sum_j W_j(\mathbf{x}) I_p(\mathbf{x} - \mathbf{x}_j; d, w) \tag{4.2.13}$$

is an entire calculated image. The function W_j is defined to be equal to 1 if $\mathbf{x}$ is inside the Voronoi area of particle j, and 0 otherwise. Minimizing the new χ^2 with respect to positions $\mathbf{x}_j$ allows us to obtain the particle centers with sub-pixel resolution. This is equivalent to solving

$$\frac{\partial}{\partial \mathbf{x}_j}\chi^2(\mathbf{x}_j; d, w) = 0 \tag{4.2.14}$$

for the $\mathbf{x}_j$. Now, we adjust d and w by solving simultaneously

$$\frac{\partial}{\partial d}\chi^2(\mathbf{x}_0; d, w) = 0 \tag{4.2.15}$$

for d and

$$\frac{\partial}{\partial w}\chi^2(\mathbf{x}_0; d, w) = 0\,, \tag{4.2.16}$$

for w. With these new, improved values of d and w, we reminimize χ^2 with respect to $\mathbf{x}_j$, which finally gives us the particles positions. This process is repeated several times until achieving convergence.

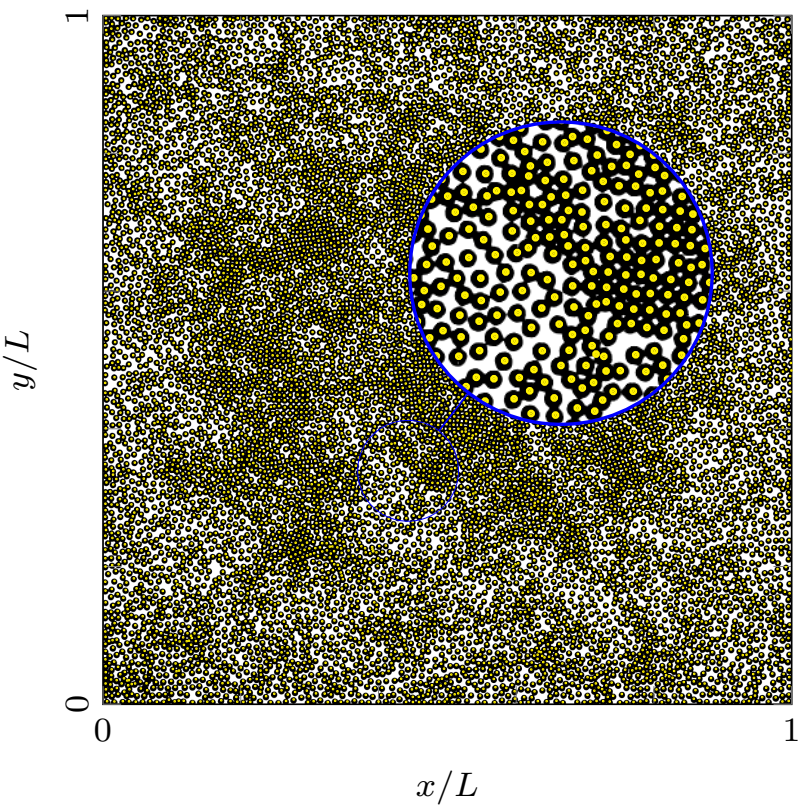

Figure 4.7: Particle detection on a sample image, at $\Gamma = 4.5$, where yellow dots are particles detected. A close-up to a section of the image is included in the inset.

Our current version of this algorithm (PTrack2 [50]) is implemented in C++ and optimized through CUDA [51, 52], which allows for faster calculations despite the considerably large

number of particles that we need to detect ($N \sim 10^4$). A small cluster of three computers is used in order to enhance efficiency, and decrease even further the time of execution of the program: for a single acquisition of 3000 images, the detection process takes $\sim 15\,\text{min}$. An example of the particles detected for a single image is shown in Figure 4.7.

4.2.2 Particle tracking

Since we require the time evolution of certain quantities of interest in our system, we need to track the particles over time. Once we have the location of particles in a sequence of images, in order to get their trayectories we have to match up their locations on each image. This requires determining which particle in a given frame most likely corresponds to one in the preceeding frame. Since our particles are indistinguishable, this likelihood can be estimated only by proximity.

A Matlab, open source code is used, elaborated by Daniel Blair and Eric Dufresne [53], and based on the algorithm by Crocker *et al.* [54]. The probability that a single Brownian particle will diffuse a distance δ in time τ is

$$P(\delta \mid \tau) = \frac{1}{4\pi D\tau} \exp\left(-\frac{\delta^2}{4D\tau}\right), \tag{4.2.17}$$

where D is the particle's self-diffusion coefficient. For an ensemble of N noninteracting particles, the probability distribution is

$$P(\{\delta_i\} \mid \tau) = \left(\frac{1}{4\pi D\tau}\right)^N \exp\left(-\sum_{i=1}^{N} \frac{\delta_i^2}{4D\tau}\right). \tag{4.2.18}$$

Maximizing $P(\{\delta_i\} \mid \tau)$, or equivalently, minimizing $\sum_{i=1}^{N} \frac{\delta_i^2}{4D\tau}$, allows us to find the most likely particle matching between consecutive images. The assignment of labels can be thought as drawing a bond between a pair of particles in consecutive images. Since calculating $P(\{\delta_i\} \mid \tau)$ for all posible combinations is impractical (it would require $\mathcal{O}(N!)$ calculations), we consider only those bonds shorter than a characteristic length Δ, corresponding to the maximum distance a particle can travel between consecutive images. This reduces considerably the calculation time: if each particle has M possible candidates within a radius Δ in the next image (with $M \ll N$), then $\mathcal{O}(M!)$ operations are needed.

Due to the high number of particles in the system ($N \sim 10^4$), the combinatorics in order to track them during a whole acquisition of 3000 images (equivalenty, 6 s in recording time) are too big. To surpass this, we track particles during intervals of 200 images (400 ms). This time interval, though small, is large compared to the fast time scale of energy injection and dissipation in the system (since the vibration period of the cell is $1/f = 12.5\,\text{ms}$) and therefore still allows to obtain robust statistics. Figure 4.8 shows the trayectories obtained for a subset of the system, in a sample image.

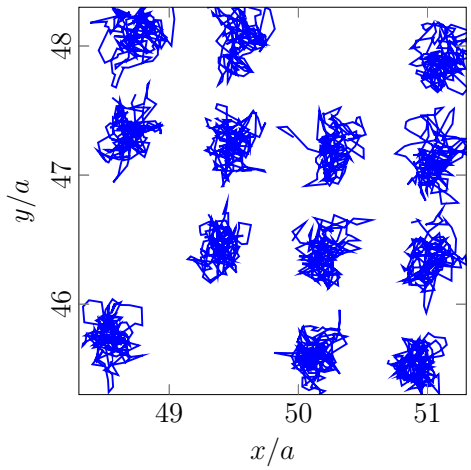

Figure 4.8: Particle trayectories of a selected subset of the system in the solid phase, from $t = 0\,\mathrm{s}$ to $t = 0.398\,\mathrm{s}$ for a sample image at $\Gamma = 6.0$.

Chapter 5

Order parameter and phase transition

One of the most remarkable properties of this setup is the existence of a liquid-to-solid-like phase transition (see Figure 5.1). When the vibration amplitude surpasses a certain threshold, a stable crystalline cluster is formed, coexisting with a fluid phase.

In this chapter, we present a characterization of order in our experiment, reported in previous work [11, 13]. With that purpose, in Section §5.1, we define a bond-orientational order parameter, which allows us to classify particles in the solid and liquid phase. Then, in Section §5.2, the phase transition is characterized through a global average of the bond-orientational order parameter.

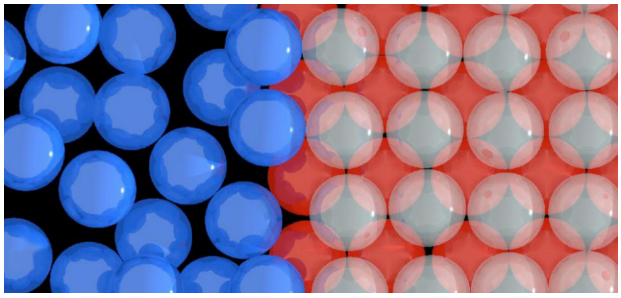

(a)

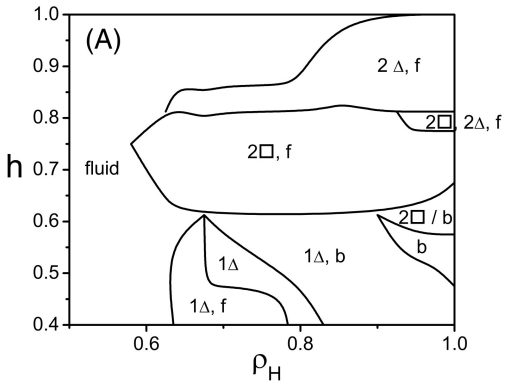

(b)

Figure 5.1: (a) 3D rendering of particle positions showing phase coexistence, with a close up to the interface between the liquid (blue) and solid (red and white) phases. (b) Phase diagram for the granular quasi-2D system, as a function of density and height of the cell, with $A = 0.15a$ and $f = 75\,\mathrm{Hz}$. The observed phases are fluid (f), single-layer hexagonal ($\triangle$), buckling (b), two-layer square ($2\square$), and two-layer hexagonal ($2\triangle$), with coexistence regions between neighbouring phases where, for example, two hexagonal layers coexist with a fluid ($2\triangle$, f) [55, 56].

5.1 Bond-orientational order parameter and particle classification

The phase transition in our setup is described by a bond-orientational order parameter, which is non-conserved and critical, coupled to the conserved, non-critical density field [11, 13]. The fourfold bond-orientational order parameter is defined as

$$Q_4^j = \frac{1}{N_j} \sum_{s=1}^{N_j} e^{4i\theta_s^j}, \tag{5.1.1}$$

where N_j corresponds to the number of nearest neighbors of particle j, and θ_s^j is the angle between the neighbor s of particle j and the x axis (See Figure 5.2). For a particle in a square lattice, $\left|Q_4^j\right| = 1$, with the complex phase measuring the orientation of the square lattice with respect to the x axis.

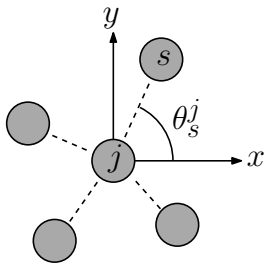

Figure 5.2: Angle θ_s^j in the definition of Q_4^j.

As in previous works [12, 57], we find that the distribution of $\left|Q_4^j\right|$ is bimodal, with a wide maximum at $\left|Q_4^j\right| \approx 0.25$, and a much narrower one at $\left|Q_4^j\right| \approx 0.95$. The former widens and decreases in height as Γ increases, while the latter increases in height as Γ goes beyond the phase transition. The local minimum between these two peaks, at $\left|Q_4^j\right| \approx 0.7$, hints the possibility of distinguishing between particles in the solid and liquid phase (See figure 5.3).

In Figure 5.4a, we show the standard deviation of $\left|Q_4^j\right|$, $\sigma_{\left|Q_4^j\right|}$, versus $\left\langle\left|Q_4^j\right|\right\rangle$, the time-average of $\left|Q_4^j\right|$, for three different accelerations. For lower and intermediate Γ, most particles are in the liquid phase, with some particles occasionally condensing into small, short-lived solid clusters. Well above the transition, a considerable amount of particles stay in the solid phase for most of the time series. At intermediate and high accelerations, a large fraction of particles fluctuate between both phases randomly, as manifested by the larger measured $\sigma_{\left|Q_4^j\right|}$. This behaviour allows us to classify particles as liquid if they satisfy $\left\langle\left|Q_4^j\right|\right\rangle \leq 0.4$, or solid, if $\left\langle\left|Q_4^j\right|\right\rangle \geq 0.7$.

Figure 5.4b displays two typical time series of $\left|Q_4^j\right|$, for a particle in the solid phase, and one in the liquid phase, both for an acquisition at $\Gamma = 6.0$. The particle in the solid phase has a high average $\left|Q_4^j\right|$, whereas the particle in the liquid phase has a lower average $\left|Q_4^j\right|$, with both showing fluctuations.

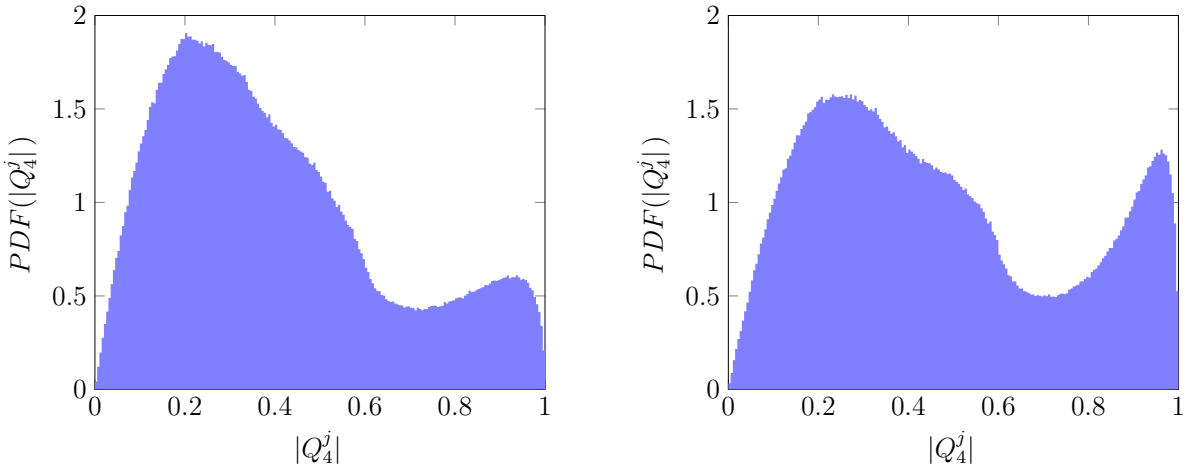

(a) (b)

Figure 5.3: Normalized histograms of $\left|Q_4^j\right|$ for two accelerations of the system: (a) $\Gamma = 2.0$, and (b) $\Gamma = 5.0$. The distributions show peaks at $\left|Q_4^j\right| \sim 0.25$ and $\left|Q_4^j\right| \sim 0.95$. The latter peak grows when increasing Γ. Statistics were obtained from 200 consecutive images for each Γ.

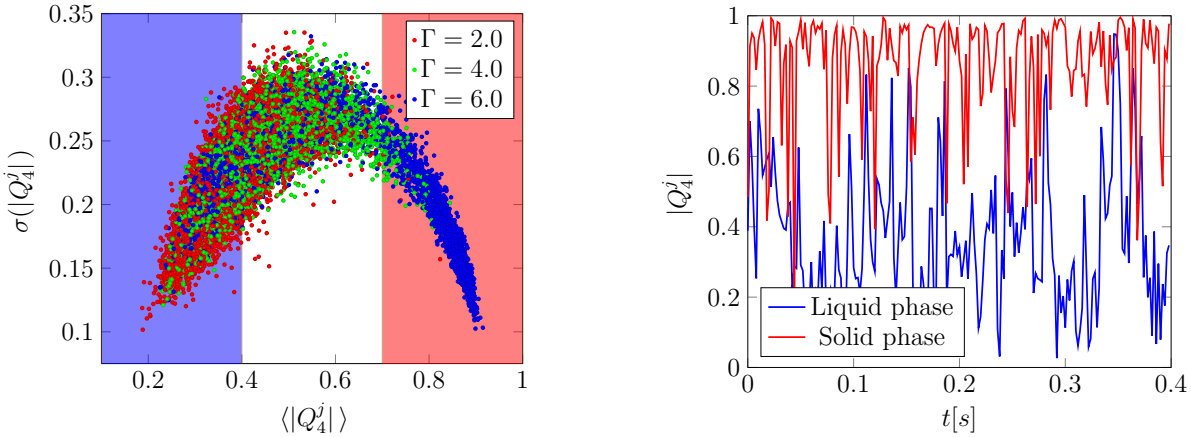

(a) (b)

Figure 5.4: (a) Mean of $\left|Q_4^j\right|$ versus its standard deviation, for different values of Γ. We classify particles in the liquid phase, if $\left\langle \left|Q_4^j\right| \right\rangle \leq 0.4$ (blue shaded area) and in the liquid phase if $\left\langle \left|Q_4^j\right| \right\rangle \geq 0.7$ (red shaded area). (b) Time-series of $\left|Q_4^j\right|$ for two sample particles, one in the liquid phase and one in the solid phase, for $\Gamma = 6.0$.

5.2 Liquid-solid-like phase transition

As we stated before, above a critical acceleration Γ_c, particles form a crystalline cluster surrounded by a liquid phase. The structure of the solid phase consists of two square lattices (with unit cell length a in each plane) interlaced, because of the quasi-2D geometry, and stabilized by the collisions with the top and bottom walls and the confining pressure exerted by the liquid phase [56]. These two layers, when projected in 2D, result in another square lattice with unit cell length $\sqrt{2}a/2$ when particles are close packed (See Figure 5.5).

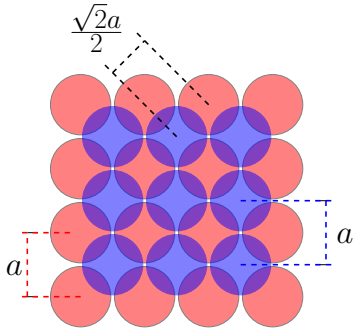

Figure 5.5: Schematic for the structure of the solid phase. It consists of two interlaced square lattices (each with unit cell length a). The proyection in 2D of this bilayer results in another square lattice, rotated 45° with respect to the original layers, and with unit cell length $\sqrt{2}a/2$.

In order to describe the phase transtition, we calculate a global Q_4, defined as

$$|\langle Q_4 \rangle| \equiv \left| \left\langle \frac{1}{N} \sum_{j=1}^{N} Q_4^j \right\rangle \right|, \tag{5.2.1}$$

where $\langle \cdot \rangle$ denotes time average. Note that $|\langle Q_4 \rangle|$ measures the average fraction of particles in the solid phase. Notably, the transition can be either continuous or discontinuous depending on the box height L_z. As reported before [12], the present configuration with $L_z = (1.94 \pm 0.02)a$ implies a second order phase transition, with the global Q_4 having a continuous critical behavior when crossing Γ_c.

In preceeding work the global Q_4 was calculated as an average of the absolute values of Q_4^j. As noted by Olivier Dauchot [58], this has the drawback of losing the phase of the complex number. Following his suggestion, we calculated the global Q_4 as the absolute value of the average of Q_4^j, as in equation (5.2.1). Figure 5.6a shows a plot of $|\langle Q_4 \rangle|$ versus the acceleration Γ, as previously calculated, along with the corresponding fit $|\langle Q_4 \rangle| = Q_4^L + C(\Gamma - \Gamma_c)^{1/2}\Theta(\Gamma - \Gamma_c)$, where $Q_4^L = Q_4^0 + B\Gamma$, and Θ is the Heaviside step function. This fit yields the critical acceleration, $\Gamma_c = 4.703 \pm 0.151$. figure 5.6b shows a plot of $|\langle Q_4 \rangle|$ as calculated now, along with the corresponding fit $|\langle Q_4 \rangle| = Q_4^0 + C(\Gamma - \Gamma_c)^{1/2}\Theta(\Gamma - \Gamma_c)$, which yields the critical acceleration $\Gamma_c = 4.698 \pm 0.025$. Although there is no substantial change in the value of Γ_c, it is evident from the figure that calculating $|\langle Q_4 \rangle|$ in this manner results in a more clean representation of the phase transition, compared with previous publications on this setup [11, 13]. It should be noted that the value of Γ_c can vary with the particle density, the height of the cell or the thickness of the ITO nano-layer.

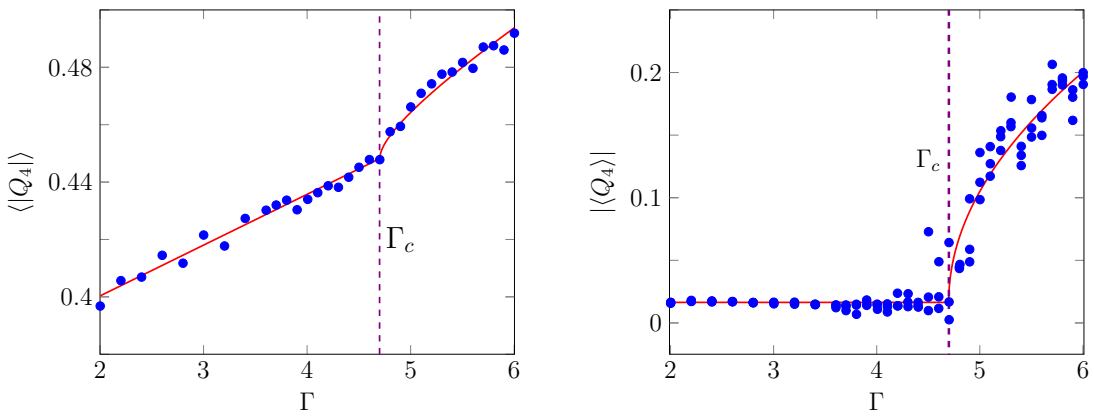

(a) (b)

Figure 5.6: Global Q_4 versus Γ as calculated as in (a) previous work and (b) present. The solid lines represent fits, and the dashed lines represent the critical acceleration Γ_c obtained from such fits. The fit used in (a) corresponds to $|\langle Q_4 \rangle| = Q_4^L + C(\Gamma - \Gamma_c)^{1/2}\Theta(\Gamma - \Gamma_c)$, where $Q_4^L = Q_4^0 + B\Gamma$ and the adjusted values are $\Gamma_c = 4.703 \pm 0.025$, $Q_4^0 = 0.365 \pm 0.005$, $B = 0.018 \pm 0.001$ and $C = 0.020 \pm 0.004$, with $R^2 = 0.992$. As for (b), the fit corresponds to $|\langle Q_4 \rangle| = Q_4^0 + C(\Gamma - \Gamma_c)^{1/2}\Theta(\Gamma - \Gamma_c)$, where the adjusted values are $\Gamma_c = 4.698 \pm 0.025$, $Q_4^0 = 0.016 \pm 0.008$ and $B = 0.161 \pm 0.014$, with $R^2 = 0.957$.

In order to visualize the state of the system for different accelerations, we present in Figure 5.7 colormaps of $\left|Q_4^j\right|$ for different values of Γ. For low accelerations (figure 5.7a), the system is uniformly fluidized, with small, short-lived solid patches that become larger and more persistent with increasing Γ (figure 5.7b). As the acceleration approaches Γ_c, the length scales and lifetimes of the solid patches diverge, forming a single, more stable cluster surrounded by the liquid phase (figure 5.7c). Well past the transition, the interface between the solid cluster and the liquid phase becomes increasingly more distinct (figure 5.7d).

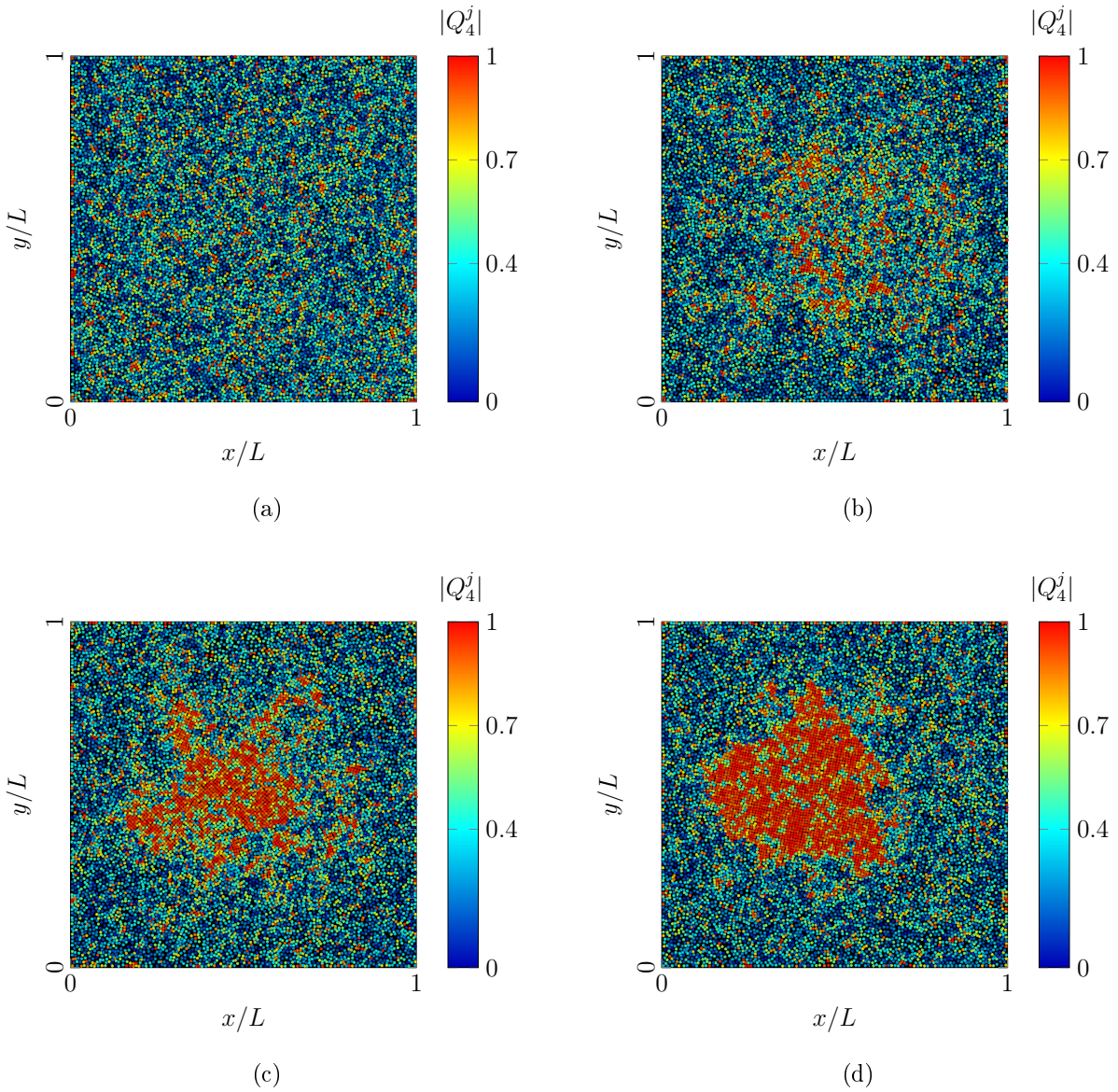

Figure 5.7: Color maps of $\left|Q_4^j\right|$ for accelerations (a) $\Gamma = 2.0$, (b) $\Gamma = 4.0$, (c) $\Gamma = 5.0$ and (d) $\Gamma = 6.0$. As the acceleration approaches the critical value, solid particles become more frequent, forming a crystalline cluster surrounded by the liquid phase.

Chapter 6

Results and analysis

In this chapter, we present the results of our experimental work. In Section §6.1 and Section §6.2, we show the attempts to describe the suppression of density fluctuations at large scales, characteristic of hyperuniformity, by means of the static structure factor and the particle number variance, respectively. The existence of finite size effects and inhomogeneities, which are inherent in our setup, will be essential to assess the best observable to characterize hyperuniformity in this particular system. In Section §6.3 we study the transport of the grains in the experiment. The criterion established in Chapter 5, which grants us a means to classify particles as solid or liquid, allows us to calculate the mean square displacement for both phases separately. Finally, in Section §6.4, we make a brief summary of a model proposed to describe the dynamic generation of hyperuniform states in our setup, through the interaction of solid patches with high friction and density waves.

6.1 Static Structure Factor

In equation (2.1.16), we presented the usual definition of the static structure factor. However, in general, $\langle\hat{\rho}(\mathbf{k})\rangle \neq 0$, because boundary conditions induce inhomogeneities in our experiment. In order to eliminate this effect [13], we calculate the structure factor as

$$S(\mathbf{k}) = \frac{\left\langle \left|\widehat{\rho}(\mathbf{k}) - \langle\widehat{\rho}(\mathbf{k})\rangle\right|^2 \right\rangle}{N} \tag{6.1.1}$$

$$S(\mathbf{k}) = \frac{\left\langle \widehat{\rho}(\mathbf{k})\widehat{\rho}^{\dagger}(\mathbf{k}) \right\rangle - \langle\widehat{\rho}(\mathbf{k})\rangle \left\langle\widehat{\rho}^{\dagger}(\mathbf{k})\right\rangle}{N}\,, \tag{6.1.2}$$

where $\langle\cdot\rangle$ denotes time averaging. Thus, having determined the particle positions $\mathbf{r}_j$ in the (x, y) plane (there is no experimental access to the z coordinate) and with the wavevectors calculated as $\mathbf{k} = \pi(n_x\hat{\imath} + n_y\hat{\jmath})/L$ ($n_x, n_y \in \mathbb{N}$), calculation of $S(\mathbf{k})$ is straightforward. All measurements of this quantity are performed in the liquid phase ($\Gamma < \Gamma_c$), where the system is isotropic, implying $S(\mathbf{k}) = S(k)$, where $k \equiv |\mathbf{k}|$. For $\Gamma > \Gamma_c$, the structure factor is not well defined because of the phase separation, as in principle the solid cluster and the liquid phase could behave differently.

Figure 6.1a shows $S(k)$ for $\Gamma = 2.0$. It has the expected behavior for fluids, but for intermediate wavelengths ($ka \sim 0.2$) a pre-peak is observed [13], which corresponds to a large

wavelength structure of size $\sim 15d$. The term pre-peak refers to this peak being at lower wavenumber than the one corresponding to the first coordination shell, which occurs at $ka = 2\pi$. Figure 6.1b shows a close-up to small wavenumbers of the structure factor, for different values of Γ below the transition. Notably, when increasing Γ, the pre-peak grows in height as it moves to slightly lower k. The curves show a clear decrease in $S(k)$ when $k \to 0$, which appears to accentuate when increasing Γ.

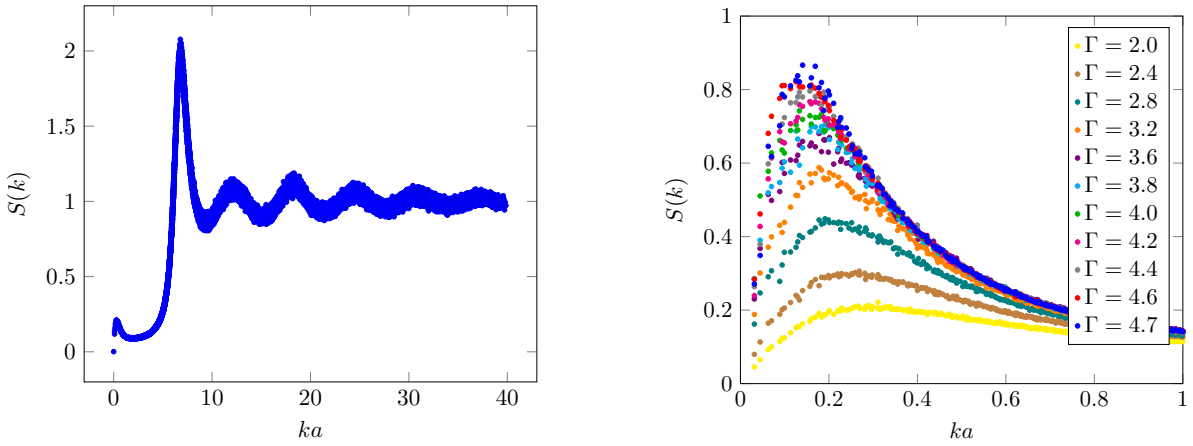

(a) (b)

Figure 6.1: (a) $S(k)$ for $\Gamma = 2.0$, showing the expected behavior for fluids, save for a pre-peak for intermediate wavelengths ($ka \sim 0.2$). (b) Close-up to small wavenumbers of $S(k)$ for different values of Γ. The pre-peak grows when increasing the acceleration, and displaces to slightly smaller wavenumbers.

Figure 6.2a shows, for a subset of Γ below the transition, the structure factor for small wavenumbers, fitted according to

$$S(k) = S_0 + S_1(ka)^{\alpha}\,, \tag{6.1.3}$$

where $\alpha = 1.12$ is a fixed exponent, obtained through fits of the structure factor calculated from numerical solution of a theoretical model (See Section §6.4). This is due to the lack of sufficient statistics in order to obtain a unique exponent from a simultaneous fit of the experimental $S(k)$ for every Γ. The range for the fits is chosen to be $[k_{\min}a, 0.65 \cdot k_{\max}a]$, where $k_{\min}$ is the minimun possible wavenumber, and $k_{\max}$ is such that $S(k_{\max})$ represents the pre-peak for a fixed Γ. To obtain $(k_{\max}, S(k_{\max}))$, the whole $S(k)$ curve is fitted for every Γ using a rational polynomial function, extracting the maximum from this fit. In a manner consistent with the increase in height of the pre-peak, the slope S_1 also increases when approaching the transition. Notably, the scaled offset S_0/S_1, shown in Figure 6.2b, vanishes at the critical acceleration, which is a clear signature of a hyperuniform state.

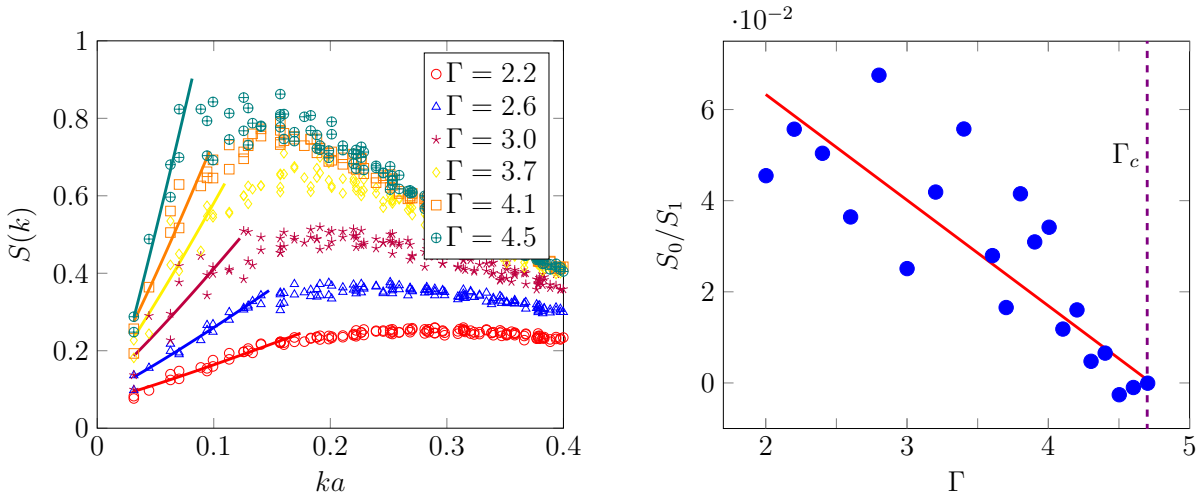

(a) (b)

Figure 6.2: (a) Static structure factor for small wavenumbers, with the corrsponding fit according to $S(k) = S_0 + S_1(ka)^\alpha$, with $\alpha = 1.12$. The fits were performed in the interval $[k_{\min}a, 0.65 \cdot k_{\max}a]$, where $k_{\min}$ is the minimun possible wavenumber, and $k_{\max}$ is the position of the maximum $S(k_{\max})$ for each Γ. (b) Scaled offset S_0/S_1 as a function of Γ, with the solid line corresponding to a linear fit passing through Γ_c. As the acceleration approaches its critical value (represented by the dashed line), the offset vanishes, which is a clear signature of a hyperuniform state.

6.2 Particle number variance

In order to quantify spatial correlations in real space, we measure the average number of particles $\langle N \rangle$ and its variance σ_N^2 in square windows of side ℓ, with the variance defined as usual,

$$\sigma_N^2(\ell) = \left\langle N(\ell)^2 \right\rangle - \langle N(\ell) \rangle^2 \ . \tag{6.2.1}$$

We must remark that for ordered systems such as regular lattices, the window shape and orientation is relevant when measuring density fluctuations through the particle number variance. Indeed, the behavior of σ_N^2 changes dramatically depending on these characteristics, and can lead to wrong assumptions on the hyperuniformity of the system [59]. Given the isotropy of our particular system, this should not be a concern.

The calculation of σ_N^2 is done as follows: for each image, we compute the number of particles in square windows with sizes ranging from $a \times a$ to $80a \times 80a$. In order to reduce the effect of spatial inhomogeneities, each square window of size ℓ is displaced throughout the entire image (excluding $10a$ at each border), which gives us an spatial average of N for that image, for each ℓ. Then, for the set of images at a fixed Γ we determine the time average $\langle N \rangle$ over all images (for each window size ℓ) and thus, its variance, σ_N^2. Figure 6.3 shows $\sigma_N^2(\ell)$ versus ℓ for different values of Γ below the critical point.

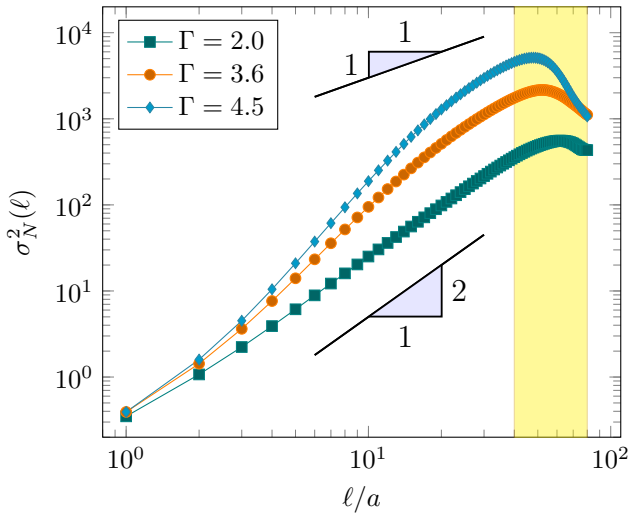

Figure 6.3: Particle number variance as a function of window size, for different values of Γ. The slopes depicted represent the expected σ_N^2 scaling in a classical disordered system, $\beta = 2$,and a hyperuniform class I system, $\beta = 1$. The yellow area represents the range where hyperuniformity should be observed if present. It ranges between the maximum window size, $\ell = 80a$, and window size associated with the pre-peak observed in the structure factor, $\ell \sim 40a$, which is considered to be the minimum length scale for the suppression of density fluctuations to be observed.

Characterizing hyperuniformity through the particle number variance requires σ_N^2 to grow slower than the window volume (in 2D, the area ℓ^2) for large ℓ. In order to observe this feature, it is necessary to have a full scale separation between the system size and the large wavelengths for which the suppression of density fluctuations occurs. This is not the case in our experiment. First, the decay of the structure factor occurs for wavenumbers below the pre-peak, around $ka \sim 0.08$ for Γ close to the transition, which translates to a window size of $\ell \sim 40a$. Second, the variance must vanish for a window equal to the system size, which is $L = 100a$, and in our calculations we excluded $10a$ per border in order to reduce the effect of boundary conditions, thus resulting in a maximum window size of $\ell = 80a$. The competition between these two factors leaves us with a negligible range in between that is insufficient to observe the large scale behavior of σ_N^2. Thus, it is not possible to describe hyperuniformity in our system through the particle number variance.

It must be noted that for window sizes $\ell \sim 10a$, the variance at $\Gamma = 2.0$ has the expected scaling for disordered systems ($\sigma_N^2 \sim \ell^2$). However, when increasing the acceleration, the fluctuations at this scale seem to increase as well. This could be a signature of giant local density fluctuations, which have been found in coexistance with hyperuniformity in a concurrent work [60].

Experimental values of the structure factor are used to produce synthetic σ_N^2 data for different system sizes, through a discrete version of equation (2.1.85), for square windows (see Supplementary Information of [61], for further details). The results show the same feature observed experimentally: the size of our experimental setup does not provide a sufficient scale separation in order to describe hyperuniformity through σ_N^2. Indeed, the cell would need to

have lateral dimensions 10 times larger, which would mean a cell the size of the optical table that currently supports the experiment (See Figure 6.4).

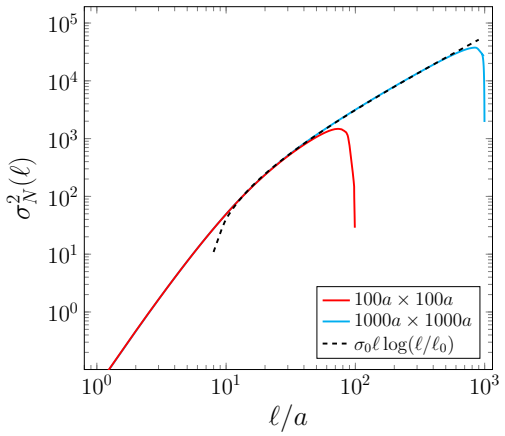

Figure 6.4: Particle number variance, σ_N^2, obtained from synthetic data for two different cell sizes. It shows that it is impossible to observe hyperuniformity in a system the size of our experimental setup (of dimensions $100a \times 100a$), and it may only be observed for very large systems. The dashed line shows the expected law for a hyperuniform 2D system with $\alpha = 1$.

Molecular dynamics (MD) simulations for a larger system, performed by colaborator Marcelo Guzmán [61], show that σ_N^2 indeed grows slower than the area of the window for large ℓ (See Figure 6.5b). Surprisingly, however, this occurs not only at Γ_c, but also for finite distances to the critical point, $\varepsilon \equiv (\Gamma_c - \Gamma)/\Gamma_c \neq 0$, which would imply that the system is hyperuniform not just at the phase transition. On the other hand, fitting the structure factor from the simulations using equation (6.1.3) and calculating the offset S_0/S_1 yields the same results as in the experiments, with S_0/S_1 only vanishing at the critical point (see Figure 6.5a).

Figure 6.6 presents the normalized particle number variance, $\sigma_N^2/(\ell/a)^2$, corresponding to synthetic values of σ_N^2 generated from the simulations, for an infinitely large system ($L \to \infty$). In order to produce this data, the particle number variance is obtained through equation (2.1.85) using $S(k)$ from the simulations for different values of S_0/S_1, which in turn represent different distances to the critical point (for further details, see Supplementary Information for [61]). As expected, $\sigma_N^2/\ell^2 \sim \ell^{-1}$ at $\varepsilon = 0$, indicating hyperuniformity. However, for finite $\varepsilon \neq 0$, the normalized particle number variance first behaves as $\sigma_N^2/\ell^2 \sim \ell^{-1}$ to finally reach a constant value, which is consistent with the finite values of S_0/S_1. The crossover between these two regimes takes place at quite large values of ℓ, which can be larger than the system size. Consequently, for finite size systems, σ_N^2 can be misleading to characterize hyperuniformity.

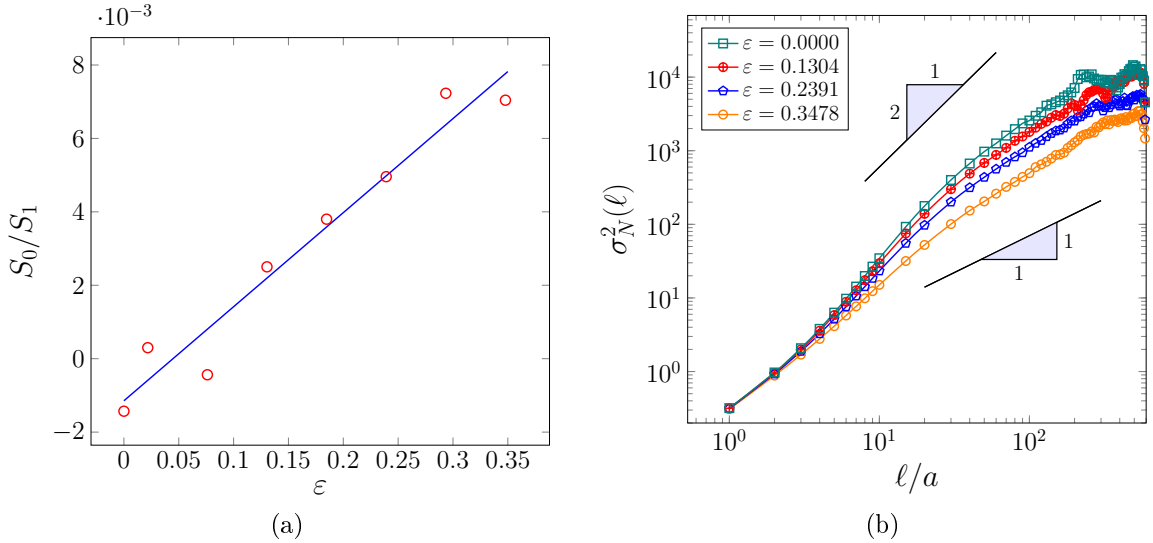

Figure 6.5: Results from MD simulations for a system of size $600a \times 600a$. (a) Scaled offset S_0/S_1 as a function of ε, where the solid line is a linear fit. As in the experimental results, S_0/S_1 vanishes at the critical point. (b) Particle number variance for different values of ε. It shows the expected scaling for hyperuniformity at the critical point, but also for finite values of $\varepsilon \neq 0$. The slopes depicted represent the expected σ_N^2 scaling in a classical disordered system, $\beta = 2$,and a hyperuniform class I system, $\beta = 1$.

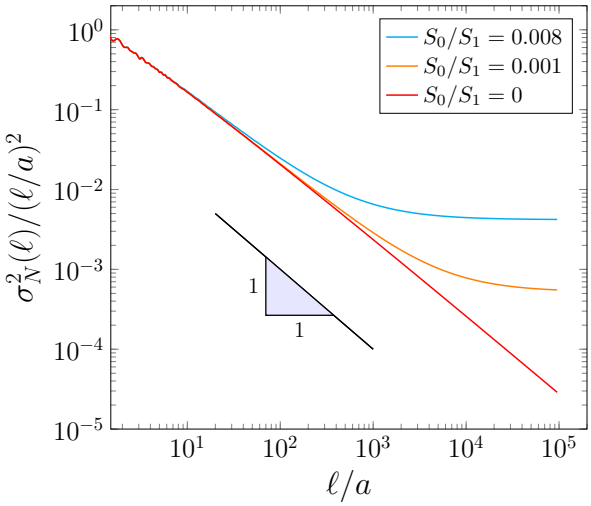

Figure 6.6: Normalized particle number variance, σ_N^2/ℓ^2, for an infinitely large system ($L \to \infty$), obtained from synthetic data generated using the MD simulation values of $S(k)$, for different values of S_0/S_1. For finite distances to the critical point, σ_N^2/ℓ^2 first has a scaling consistent with hyperuniformity ($\sigma_N^2/\ell^2 \sim \ell^{-1}$, the slope depicted in the figure), but then reaches a constant value for larger window sizes. Hence, for finite size systems, σ_N^2 can indicate erroneously that the system is hyperuniform.

6.3 Mean square displacement

As we introduced in section Section §5.1, a single particle j can be classified as solid or liquid depending on the value of the time-average, $\langle |Q_4^j| \rangle$. This classification allows us to calculate the MSD for each phase separately. We remark that an additional criterion consisting in an upper bound for the standard deviation, $\sigma_{|Q_4^j|}$, shows no substantial difference in the calculation of the MSD for our system.

The MSD is directly calculated using

$$\left\langle (\mathbf{r}(t) - \mathbf{r_0})^2 \right\rangle = \frac{1}{N} \sum_{j=1}^{N} (\mathbf{r_j}(t) - \mathbf{r_{0j}}) \,. \tag{6.3.1}$$

The results below were obtained from videos of 3000 images at sample rate $f_2 = 500\,\mathrm{Hz}$. The videos were divided into intervals of 200 images, due to the extremely high combinatorics needed to track all the particles during a whole acquisition. For every interval, the MSD is calculated, and then averaged over the intervals in order to get better statistics.

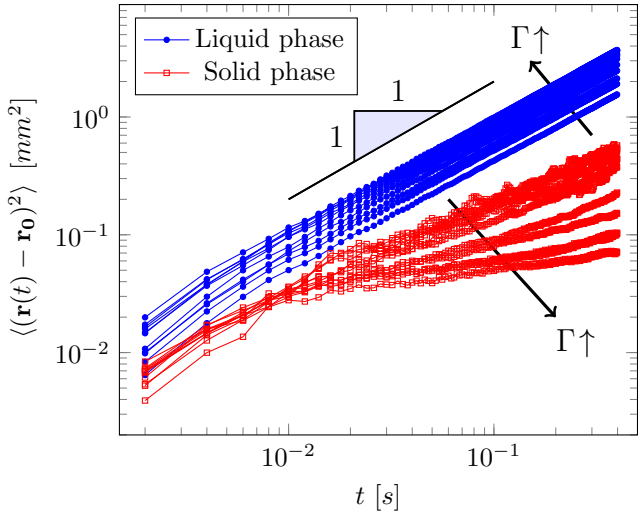

Figure 6.7: MSD as a function of time, for different values of Γ. The slope depicted represents the scaling for difussive transport. The liquid phase shows diffusion, with a diffusion coefficient that increases with the acceleration. Contrarily, the solid phase is subdiffusive; a behavior which accentuates with increasing acceleration.

Figure 6.7 shows the MSD as a function of time for solid and liquid phases and for different values of Γ. We find that the behaviour is radically different for the two phases. The former exhibits diffusion, which grows with the acceleration, while the latter shows subdiffusive dynamics. When we look at a typical trajectory of a particle, we observe that the displacements for solid particles are confined to a small region, in contrast to liquid particles, which have greater displacements and move more freely (See figure 6.8). The subdiffusion existing in the solid phase is a result of caging from the surrounding particles, and from enhanced friction, which arises from the repeated rapid collisions with the top and bottom walls. It can be modeled by a very small diffusion coefficient that seems to decrease when increasing Γ.

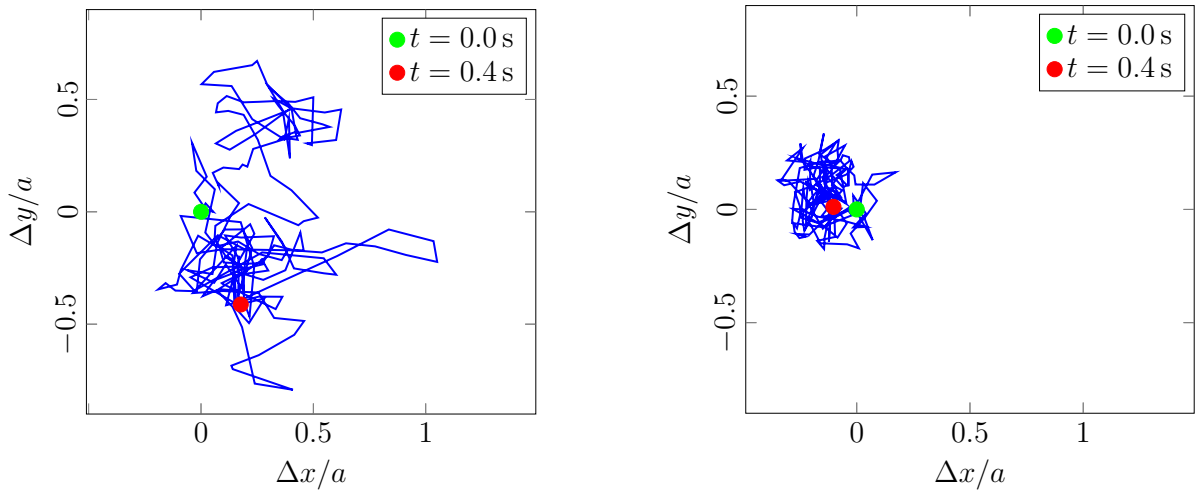

(a) (b)

Figure 6.8: Trayectories for two sample particles at $\Gamma = 5.0$: (a) liquid particle, and (b) solid particle. Note the difference in the scale of the displacements, which hints the diffusion present in the liquid phase, and the caging experienced by particles in the solid phase.

For the liquid phase, we obtain the diffusion coefficients by fitting the MSD according to

$$\left\langle (\mathbf{r}(t) - \mathbf{r_0})^2 \right\rangle = 4Dt\,, \tag{6.3.2}$$

which is the same as equation (3.2.8), but applied to our quasi-2D case (*i.e.* $n = 2$). In Figure 6.9a we present the diffusivity for the liquid phase, for different values of Γ. As it would be expected, diffusion grows with the acceleration, although there appears to be a change in behavior past Γ_c. Figure 6.9b shows the diffusion as a function of $(A\omega)^2$, which is a measure of the energy (per unit of mass) injected in the system. Naturally, diffusivity increases with the injection of energy, but it seems to saturate past the transition. This saturation is a direct effect of the enhanced friction in the coexistance regime, which we mentioned before.

In figure 6.9c we present the granular temperature (per unit mass) T versus the acceleration Γ, with T calculated as:

$$T = \frac{\sum_{j=1}^{N} \left\langle v_j^2 \right\rangle}{N}\,, \tag{6.3.3}$$

where $v_j^2 = v_{xj}^2 + v_{yj}^2$, and the brackets denote time averaging. An extrapolation of this temperature to lower accelerations should not be expected to satisfy $T(\Gamma = 1) = 0$, since there is a minimum non-unit acceleration needed in order to keep the system fluidized, *i.e.* the energy injection must balance the barrier imposed not only by gravity, but also by friction and contact forces between the particles. Figure 6.9d shows the diffusion coefficient as a function of the square root of the granular temperature, where a linear relation is clearly observed. This behavior is consistent with theoretical predictions and other experimental results for fluidized granular systems [43, 30, 31, 32, 33], where

$$D \propto T^{1/2}\,. \tag{6.3.4}$$

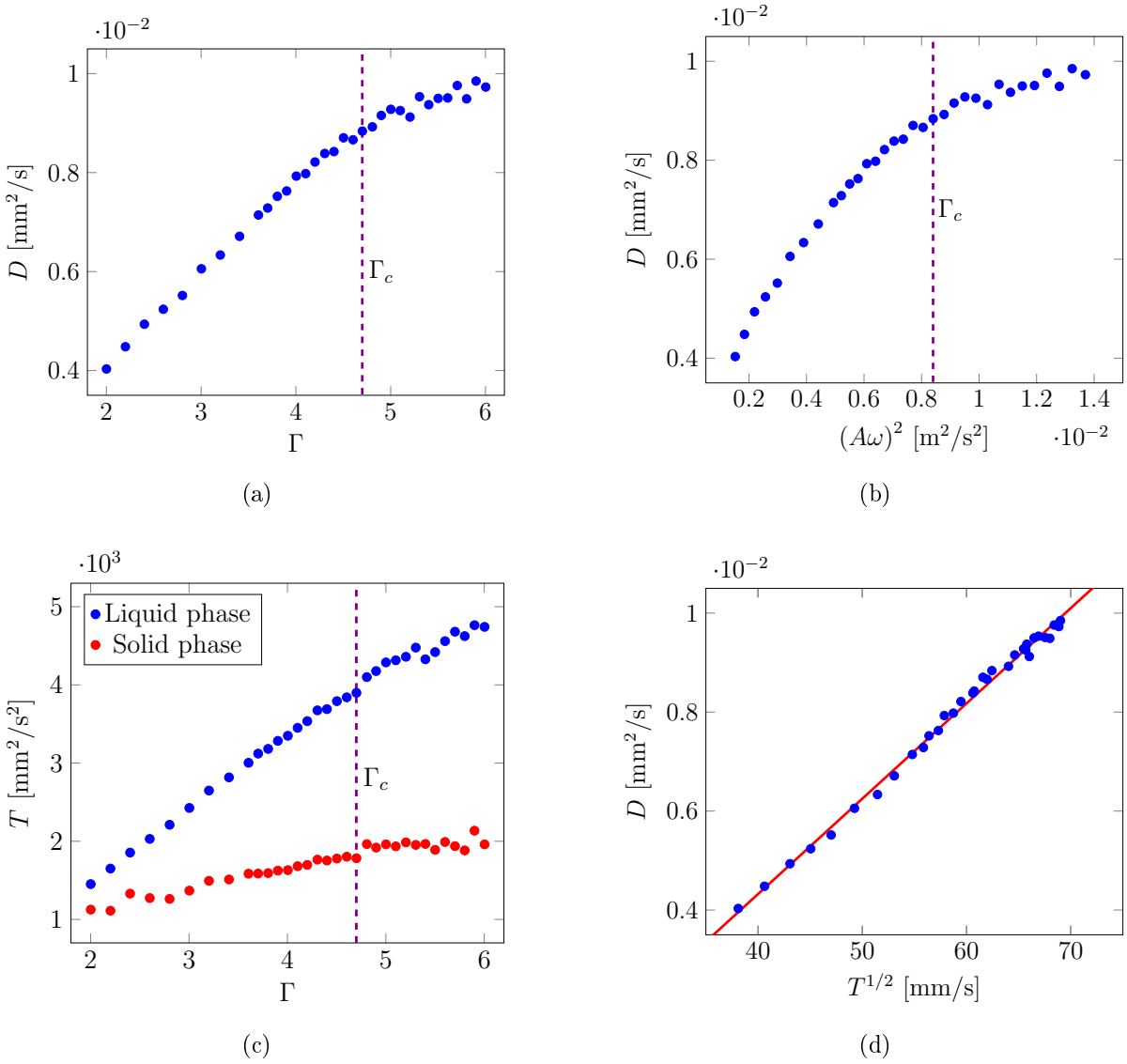

Figure 6.9: (a) The diffusion coefficient, D, for different values of the adimensional acceleration Γ. (b) Diffusion coefficient, D, as a function of energy (per unit mass) injected in the system,$(A\omega)^2$. D seems to saturate past the phase transition ($\Gamma > \Gamma_c$), due to the increased dissipation in the collisions between the grains and the top and bottom walls. (c) Granular temperature, T, as a function of the adimensional acceleration, Γ, showing the difference of temperature between the liquid and solid phase. Increasing the amplitude of vibration results in larger transfer of energy to the motion of the particles. (d) The diffusion coefficient, D, versus scaled granular temperature, $T^{1/2}$. The solid line represents a linear fit, showing a correspondance with the expected scaling, $D \propto T^{1/2}$. In (a), (b), (c), the dashed line represents the critical point.

6.4 Interpretation and model

As we previously discussed, solid patches form in the liquid phase as the system approaches the critical acceleration, with their lifetimes and length scales diverging at the transition. Our hypothesis is that these sub-diffusive structures block the propagation of density waves, effectively suppressing density fluctuations at Γ_c. A schematic representation of these interactions is presented in Figure 6.10.

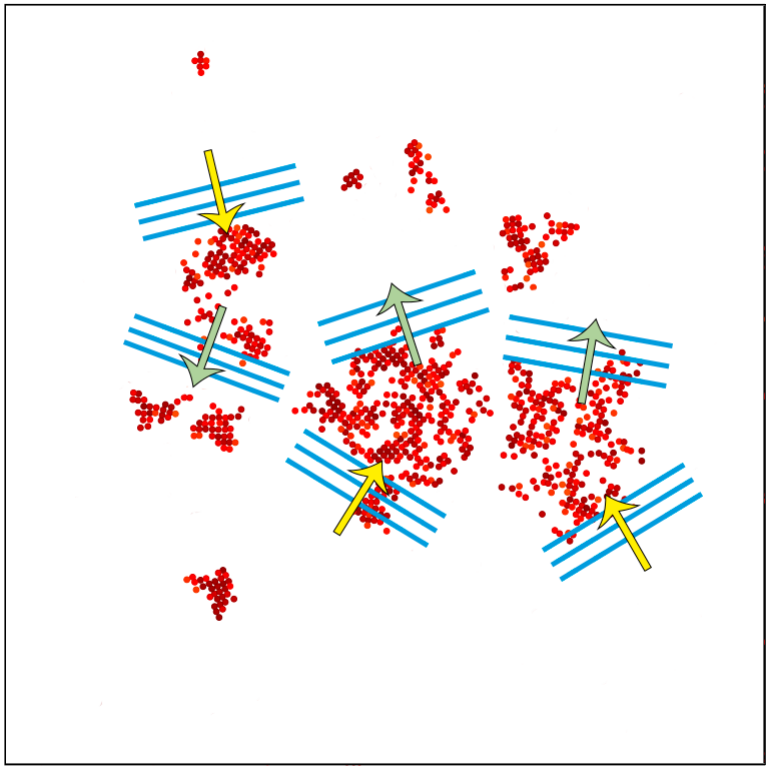

Figure 6.10: Schematic representation of the interaction between density waves and solid patches. The sub-diffusive solid patches block the propagation of density fluctuations, and completely suppress them at the crititical point.

From this interpretation, a model was proposed by our colaborators Rodrigo Soto and Nestor Sepúlveda, in which density evolves by diffusion [61]

$$\frac{\partial \rho}{\partial t} = \boldsymbol{\nabla} \cdot (D \boldsymbol{\nabla} \rho + \boldsymbol{\eta}) \,, \tag{6.4.1}$$

where $\boldsymbol{\eta}$ is a fluctuating mass flux, modeled as a white noise. The diffusion coefficient, D, depends on a local order field ψ (related to Q_4), which is described by a critical equation

$$\frac{\partial \psi}{\partial t} = \mu \boldsymbol{\nabla}^b \psi - \nu \psi + \xi \,, \tag{6.4.2}$$

where ν measures the distance to the critical point (and is related to Γ), μ accounts for spatial coupling of ψ, and ξ is a white noise. The order parameter ψ presents fluctuations that grow when approaching the transition and, hence, large values of ψ correspond to the solid phase. To account for the sub-diffusive behaviour found experimentally for the solid patches,

the diffusion coefficient is modeled as $D = D_0 e^{-\lambda\psi^2}$, thus taking finite values in the liquid phase while vanishing asymptotically for the solid phase. Therefore, this model retains the principal features of our experiment, namely the existence of a critical non-conserved order parameter, which controls the diffusion of the conserved non-critical density field

Numerical solution of the model reproduces the experimental results. Figure 6.11b presents the particle number variance for different values of ν. As in the experiment, due to finite size effects, it is impossible to observe the large scale beahvior of σ_N^2. On the other hand, the suppression of density fluctuations is indeed observed through the structure factor. Calculation of $S(k)$, and the posterior fitting through equation equation (6.1.3) results in the scaled offset S_0/S_1 also vanishing when approaching the transition (see Figure 6.11a), but for a small, finite value of $\nu \neq 0$, due to renormalization effects.

The exponent $\alpha = 1.12 \pm 0.15$ (used to fit the experimental $S(k)$) is obtained from the structure factor fits in the numerical solution of the model, by imposing the same α for all values of ν. We should remark that it is not possible to make a categorical statement regarding the hyperuniformity class of our system, given the numerical precision of α obtained and the impossibility of observing the large-scale behavior of σ_N^2 in the experiment.

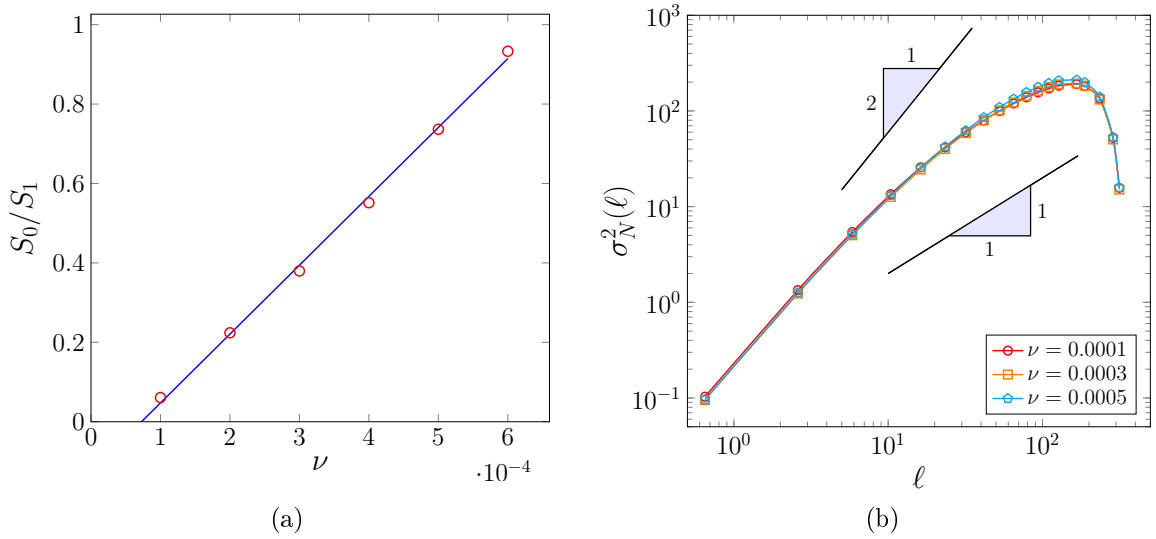

(a) (b)

Figure 6.11: Results from the numerical solution of the model. (a) Scaled offset S_0/S_1 obtained as a function of the distance to the critical point. The solid line is a linear fit showing that S_0/S_1 vanishes when approaching the transition, which reproduces the hyperuniformity found experimentally. (b) Particle number variance for different values of ν. As in the experiment, it is impossible to observe the large-scale behavior of σ_N^2. The slopes depicted represent the expected σ_N^2 scaling in a classical disordered system, $\beta = 2$,and a hyperuniform class I system, $\beta = 1$.

Chapter 7

Conclusions

In this thesis, we have studied the density fluctuations in a vibrated granular quasi-2D system, with the primary objective of demonstrating the presence of dynamically generated hyperuniform states. Our experimental setup, presented in section §4.1, shows a liquid-to-solid-like phase transition that is characteristic of this geometry. Past a critical acceleration Γ_c, a solid cluster with crystalline structure coexists with a surrounding liquid phase. Particle positions are obtained from acquired images, and then analyzed in order to quantify density fluctuations and other statistics. Previously reported characterization of the phase transition is a fundamental tool in this thesis, as it helps us characterize local order and identify the critical acceleration.

In the first part of our results, we studied density fluctuations in Fourier space by means of the static structure factor, $S(k)$. This quantity shows a pre-peak for intermediate wavelengths, that grows when increasing Γ. However, for lower wavenumbers it is observed that $S(k)$ decreases when $k \to 0$, which hints the existence of hyperuniformity. Indeed, after fitting the data according to $S(k) = S_0 + S_1 k^\alpha$, with $\alpha = 1.12$, we found that the scaled offset S_0/S_1 vanishes at the transition, which is a clear signature of a hyperuniform state.

Secondly, we looked at density fluctuations of the system in real space, through the particle number variance. In hyperuniform states, σ_N^2 must grow slower than the window volume (area, in our quasi-2D geometry) for large window sizes, but this behavior is impossible to observe in our system. Our experimental setup lacks a significant scale separation between the system size and the large scales at which density fluctuations are observed to be suppressed through the structure factor. Synthetic data generated from the experimental structure factor suggests that in order to observe the scaling of σ_N^2, the system would have to be of the size of the optical table that currently supports the quasi-2D cell in our setup, which is practically unfeasible.

Notably, the finite size effects and boundary inhomogeneities that frustrated our attempt of observing hyperuniformity through σ_N^2 are also present in the usual definition of the structure factor (equation (2.1.16)), due to the fact that in general $\langle \hat{\rho}(k) \rangle \neq 0$. Nonetheless, equation (6.1.2) used to calculate $S(k)$ (reported previously [13]) has the advantage of cancelling out these effects, which results in the structure factor being remarkably isotropic. Additionally, a drastic change in the large-scale behavior of σ_N^2 (for an infinitely large system, generated from MD simulation values of $S(k)$) indicates that the particle number variance

can lead to erroneous assumptions of hyperuniformity, for finite size systems. On the contrary, the analysis of the structure factor is robust to detect hyperuniformity. This specific feature is what makes $S(k)$, rather than σ_N^2, the ideal observable to identify hyperuniform states in systems of these characteristics.

In the third part of our results, we studied diffusion in our system by calculating the mean square displacement for both phases separately. The classification of particles into solid or liquid phases was done through a criterion established on the time-average of the absolute value of the local order parameter, $\langle |Q_4^j| \rangle$. We observed that the liquid phase is diffusive, with a diffusion coefficient that increases with increasing acceleration, Γ. As for the solid phase, it shows a sub-diffusive dynamic that is enhanced when increasing the acceleration. This behavior is a consequence of caging from the particle neighbors, and the intensified friction from the rapid collisions with the top and bottom walls.

Finally, a simple model implemented by our collaborators, Rodrigo Soto and Néstor Sepúlveda, makes use of the main characteristics of the experiment, namely the evolution of the conserved density field by diffusion, controlled by a non-conserved order parameter with critical dynamics. The solid patches that form in the liquid phase have lifetimes and length scales that grow with increasing Γ, and diverge at the critical point. We propose that these sub-diffusive patches block the propagation of density fluctuations, suppressing them completely at the phase transition. Thus, the presence of highly heterogeneous friction is conjectured to be main mechanism to generate dynamical hyperuniform states. Numerical solution of this model reproduces the experimental results, as the system becomes hyperuniform when approaching the critical point, and allows to obtain the exponent $\alpha = 1.12$ used to fit the experimental $S(k)$.

Future prospects on this work include a more thorough study on the phase transition to hyperuniform states, e.g. whether or not there is universality, as different values of α have been found for different systems [6, 8, 9, 10, 29, 23]. Additionally, it remains a challenge to find alternative quantities and/or criteria to describe hyperuniformity, or ideally a more unified systematic approach, in order to eliminate the case by case search for the correct observable. This could be achieved with a better understanding on the origin of hyperuniform states. Moreover, it would be interesting to do a more thorough exploration of the phase diagram in this particular setup, in order to establish not only the dependence of the state of the system on the different parameters (frequency, cell height, etc.), but also which of these states retain the hyperuniformity. On the other hand, there is a lack of knowledge on whether this or other granular systems with dynamic hyperuniformity may present any optical properties, *e.g.* a photonic band gap. If successful, this could lead to technical applications in the optical industry, with the development of photonic band gap hyperuniform metamaterials or sampling devices with a hyperuniform structure instead of a regular array of receptors, and also in the production of powders and paints that could have novel properties such as those displayed by animals with structural color described in Section §1.1.

Bibliography

[1] Salvatore Torquato and Frank H. Stillinger. Local density fluctuations, hyperuniformity, and order metrics. *Phys. Rev. E*, 68:041113, Oct 2003.

[2] Salvatore Torquato, G Zhang, and FH Stillinger. Ensemble theory for stealthy hyperuniform disordered ground states. *Physical Review X*, 5(2):021020, 2015.

[3] Andrea Gabrielli, Michael Joyce, and Francesco Sylos Labini. Glass-like universe: Real-space correlation properties of standard cosmological models. *Phys. Rev. D*, 65:083523, Apr 2002.

[4] Marian Florescu, Salvatore Torquato, and Paul J. Steinhardt. Designer disordered materials with large, complete photonic band gaps. *Proceedings of the National Academy of Sciences*, 106(49):20658–20663, 2009.

[5] Weining Man, Marian Florescu, Kazue Matsuyama, Polin Yadak, Geev Nahal, Seyed Hashemizad, Eric Williamson, Paul Steinhardt, Salvatore Torquato, and Paul Chaikin. Photonic band gap in isotropic hyperuniform disordered solids with low dielectric contrast. *Opt. Express*, 21(17):19972–19981, Aug 2013.

[6] Yang Jiao, Timothy Lau, Haralampos Hatzikirou, Michael Meyer-Hermann, Joseph C. Corbo, and Salvatore Torquato. Avian photoreceptor patterns represent a disordered hyperuniform solution to a multiscale packing problem. *Phys. Rev. E*, 89:022721, Feb 2014.

[7] Yoël Forterre and Olivier Pouliquen. Flows of dense granular media. *Annu. Rev. Fluid Mech.*, 40:1–24, 2008.

[8] Aleksandar Donev, Frank H. Stillinger, and Salvatore Torquato. Unexpected density fluctuations in jammed disordered sphere packings. *Phys. Rev. Lett.*, 95:090604, Aug 2005.

[9] Ludovic Berthier, Pinaki Chaudhuri, Corentin Coulais, Olivier Dauchot, and Peter Sollich. Suppressed compressibility at large scale in jammed packings of size-disperse spheres. *Phys. Rev. Lett.*, 106:120601, Mar 2011.

[10] Remi Dreyfus, Ye Xu, Tim Still, L. A. Hough, A. G. Yodh, and Salvatore Torquato. Diagnosing hyperuniformity in two-dimensional, disordered, jammed packings of soft spheres. *Phys. Rev. E*, 91:012302, Jan 2015.

[11] Gustavo Castillo, Nicolás Mujica, and Rodrigo Soto. Fluctuations and criticality of a granular solid-liquid-like phase transition. *Phys. Rev. Lett.*, 109:095701, Aug 2012.

[12] Gustavo Castillo. *Order and density fluctuations in the vicinity of a granular solid-liquid-like phase transition*. Ph.D. in physics thesis, Universidad de Chile, 2012.

[13] Gustavo Castillo, Nicolás Mujica, and Rodrigo Soto. Universality and criticality of a second-order granular solid-liquid-like phase transition. *Phys. Rev. E*, 91:012141, Jan 2015.

[14] A. Gabrielli, F.S. Labini, M. Joyce, and L. Pietronero. *Statistical Physics for Cosmic Structures*. Springer Berlin Heidelberg, 2006.

[15] Adam Wax, Changhuei Yang, Vadim Backman, Kamran Badizadegan, Charles W. Boone, Ramachandra R. Dasari, and Michael S. Feld. Cellular organization and substructure measured using angle-resolved low-coherence interferometry. *Biophysical Journal*, 82(4):2256 – 2264, 2002.

[16] Yang Jiao, Hal Berman, Tim-Rasmus Kiehl, and Salvatore Torquato. Spatial organization and correlations of cell nuclei in brain tumors. *PLOS ONE*, 6(11):1–9, 11 2011.

[17] S. Warr and J.-P. Hansen. Relaxation of local density fluctuations in a fluidized granular medium. *EPL (Europhysics Letters)*, 36(8):589, 1996.

[18] Neil W. Ashcroft and N. David Mermin. *Solid State Physics*. Brooks Cole, 1976.

[19] Jean-Pierre Hansen and Ian R. McDonald. *Theory of Simple Liquids, with Applications to Soft Matter*. Academic Press, 2013.

[20] Salvatore Torquato. Hyperuniformity and its generalizations. *Phys. Rev. E*, 94:022122, Aug 2016.

[21] Salvatore Torquato. Hyperuniform states of matter. *Physics Reports*, 745:1 – 95, 2018. Hyperuniform States of Matter.

[22] Chase E Zachary and Salvatore Torquato. Hyperuniformity in point patterns and two-phase random heterogeneous media. *Journal of Statistical Mechanics: Theory and Experiment*, 2009(12):P12015, 2009.

[23] Erdal C. Oğuz, Joshua E. S. Socolar, Paul J. Steinhardt, and Salvatore Torquato. Hyperuniformity of quasicrystals. *Phys. Rev. B*, 95:054119, Feb 2017.

[24] Salvatore Torquato, A Scardicchio, and Chase E Zachary. Point processes in arbitrary dimension from fermionic gases, random matrix theory, and number theory. *Journal of Statistical Mechanics: Theory and Experiment*, 2008(11):P11019, 2008.

[25] RP Feynman and Michael Cohen. Energy spectrum of the excitations in liquid helium. *Physical Review*, 102(5):1189, 1956.

[26] G Zhang, FH Stillinger, and Salvatore Torquato. The perfect glass paradigm: Disordered hyperuniform glasses down to absolute zero. *Scientific reports*, 6:36963, 2016.

[27] Daniel Hexner and Dov Levine. Hyperuniformity of critical absorbing states. *Physical review letters*, 114(11):110602, 2015.

[28] Jaeuk Kim and Salvatore Torquato. Effect of imperfections on the hyperuniformity of many-body systems. *Physical Review B*, 97(5):054105, 2018.

[29] Gianluigi Zito, Giulia Rusciano, Giuseppe Pesce, Anna Malafronte, Rocco Di Girolamo, Giovanni Ausanio, Antonio Vecchione, and Antonio Sasso. Nanoscale engineering of two-dimensional disordered hyperuniform block-copolymer assemblies. *Phys. Rev. E*, 92:050601, Nov 2015.

[30] SS Hsiau and ML Hunt. Shear-induced particle diffusion and longitudinal velocity fluctuations in a granular-flow mixing layer. *Journal of Fluid Mechanics*, 251:299–313, 1993.

[31] Shu-San Hsiau and Yuh-Min Shieh. Fluctuations and self-diffusion of sheared granular material flows. *Journal of Rheology*, 43(5):1049–1066, 1999.

[32] RD Wildman, JM Huntley, and J-P Hansen. Self-diffusion of grains in a two-dimensional vibrofluidized bed. *Physical Review E*, 60(6):7066, 1999.

[33] Nikolai V Brilliantov and Thorsten Pöschel. Self-diffusion in granular gases. *Physical Review E*, 61(2):1716, 2000.

[34] James W Dufty, J Javier Brey, and James Lutsko. Diffusion in a granular fluid. i. theory. *Physical Review E*, 65(5):051303, 2002.

[35] James Lutsko, J Javier Brey, and James W Dufty. Diffusion in a granular fluid. ii. simulation. *Physical Review E*, 65(5):051304, 2002.

[36] Charles S Campbell. Self-diffusion in granular shear flows. *Journal of Fluid Mechanics*, 348:85–101, 1997.

[37] Adolf Fick. Ueber diffusion. *Annalen der Physik*, 170(1):59–86.

[38] H. C. Berg. *Random Walks in Biology*. Princeton University Press, 1993.

[39] GD Cody, DJ Goldfarb, GV Storch Jr, and AN Norris. Particle granular temperature in gas fluidized beds. *Powder Technology*, 87(3):211–232, 1996.

[40] Isaac Goldhirsch. Rapid granular flows. *Annual review of fluid mechanics*, 35(1):267–293, 2003.

[41] B. Andreotti, Y. Forterre, and O. Pouliquen. *Granular Media: Between Fluid and Solid*. Cambridge University Press, 2013.

[42] Isaac Goldhirsch. Introduction to granular temperature. *Powder Technology*, 182(2):130–136, 2008.

[43] N. V. Brilliantov and T. Pöschel. *Kinetic Theory of Granular Gases*. Oxford University Press, 2004.

[44] Martin Huthmann and Annette Zippelius. Dynamics of inelastically colliding rough spheres: Relaxation of translational and rotational energy. *Physical Review E*, 56(6):R6275, 1997.

[45] Steven R Dahl, Christine M Hrenya, Vicente Garzó, and James W Dufty. Kinetic temperatures for a granular mixture. *Physical Review E*, 66(4):041301, 2002.

[46] Klebert Feitosa and Narayanan Menon. Breakdown of energy equipartition in a 2d binary vibrated granular gas. *Physical review letters*, 88(19):198301, 2002.

[47] Thorlabs, Inc. `https://www.thorlabs.com/thorproduct.cfm?partnumber=PT3A/M`.

[48] Thorlabs, Inc. `https://www.thorlabs.com/thorproduct.cfm?partnumber=PR01/M`.

[49] Scott V. Franklin and Mark D. Shattuck. *Handbook of Granular Materials*. CRC Press, 2016.

[50] Juan Silva. `https://github.com/ParticleTracking2/PTrack2`.

[51] Juan Silva. Optimización de proceso de detección de partículas a partir de imágenes de video mediante paralelización. Computer science engineer thesis, Universidad de Chile, 2012.

[52] Mauricio Cerda, Cristóbal A. Navarro, Juan Silva, Scott R. Waitukaitis, Nicolás Mujica, and Nancy Hitschfeld. A high-speed tracking algorithm for dense granular media. *Computer Physics Communications*, 227:8 – 16, 2018.

[53] Daniel Blair and Eric Dufresne. `http://site.physics.georgetown.edu/matlab/`.

[54] John C. Crocker and David G. Grier. Methods of digital video microscopy for colloidal studies. *Journal of Colloid and Interface Science*, 179(1):298 – 310, 1996.

[55] Alexis Prevost, Paul Melby, David A. Egolf, and Jeffrey S. Urbach. Nonequilibrium two-phase coexistence in a confined granular layer. *Phys. Rev. E*, 70:050301, Nov 2004.

[56] P. Melby, F. Vega Reyes, A. Prevost, R. Robertson, P. Kumar, D. A. Egolf, and J. S. Urbach. The dynamics of thin vibrated granular layers. *Journal of Physics: Condensed Matter*, 17(24):S2689, 2005.

[57] Li-Hua Luu, Gustavo Castillo, Nicolás Mujica, and Rodrigo Soto. Capillarylike fluctuations of a solid-liquid interface in a noncohesive granular system. *Phys. Rev. E*, 87:040202, Apr 2013.

[58] Olivier Dauchot. Private Communication, 2018.

[59] Jaeuk Kim and Salvatore Torquato. Effect of window shape on the detection of hyperuniformity via the local number variance. *Journal of Statistical Mechanics: Theory and Experiment*, 2017(1):013402, 2017.

[60] Qun-Li Lei, Massimo Pica Ciamarra, and Ran Ni. Nonequilibrium strongly hyperuniform fluids of circle active particles with large local density fluctuations. *Science Advances*, 5(1), 2019.

[61] Gustavo Castillo, Nicolás Mujica, Néstor Sepúlveda, Juan Carlos Sobarzo, Marcelo Guzmán, and Rodrigo Soto. Hyperuniform states generated by a critical friction field. `https://arxiv.org/abs/1805.07408`, 2019.

Appendix A

Publications

- Gustavo Castillo, Nicolás Mujica, Néstor Sepúlveda, Juan Carlos Sobarzo, Marcelo Guzmán and Rodrigo Soto. **Hyperuniform states generated by a critical friction field.** *Currently under review.*

Hyperuniform states are an efficient way to fill up space for disordered systems. In these states the particle distribution is disordered at the short scale but becomes increasingly uniform when looked at large scales. Hyperuniformity appears in several systems, in static or quasistatic regimes as well as close to transitions to absorbing states. Here, we show that a vibrated granular layer, at the critical point of the liquid-to-solid transition, displays dynamic hyperuniformity. Prior to the transition, patches of the solid phase form, with length scales and mean lifetimes that diverge critically at the transition point. When reducing the wavenumber, density fluctuations encounter increasingly more patches that block their propagation, resulting in a static structure factor that tends to zero for small wavenumbers at the critical point, which is a signature of hyperuniformity. A simple model demonstrates that this coupling of a density field to a highly fluctuating scalar friction field gives rise to dynamic hyperuniform states. Finally, we show that the structure factor detects better the emergence of hyperuniformity, compared to the particle number variance.